J. Fluid Mech. (2005), *vol.* 537, *pp.* 55–89.
doi:10.1017/S0022112005004647 Printed in the United Kingdom

Linearized analysis of Richtmyer–Meshkov flow for elastic materials

By JEEYEON N. PLOHR[1] AND BRADLEY J. PLOHR[2]

[1]Theoretical Division, Equations of State and Mechanics of Materials, MS-B221, Los Alamos National Laboratory, Los Alamos, NM 87545, USA

[2]Theoretical Division, Complex Systems, MS-B213, Los Alamos National Laboratory, Los Alamos, NM 87545, USA

(Received 24 September 2004 and in revised form 21 February 2005)

We present a study of Richtmyer–Meshkov flow for elastic materials. This flow, in which a material interface is struck by a shock wave, was originally investigated for gases, where growth of perturbations of the interface is observed. Here we consider two elastic materials in frictionless contact. The governing system of equations comprises conservation laws supplemented by constitutive equations. To analyse it, we linearize the equations around a one-dimensional background solution under the assumption that the perturbation is small. The background problem defines a Riemann problem that is solved numerically; its solution contains transmitted and reflected shock waves in the longitudinal modes. The linearized Rankine–Hugoniot condition provides the interface conditions at the longitudinal and shear waves; the frictionless material interface conditions are also linearized. The resulting equations, a linear system of partial differential equations, is solved numerically using a finite-difference method supplemented by front tracking. In verifying the numerical code, we reproduce growth of the interface in the gas case. For the elastic case, in contrast, we find that the material interface remains bounded: the non-zero shear stiffness stabilizes the flow. In particular, the linear theory remains valid at late time. Moreover, we identify the principal mechanism for the stability of Richtmyer–Meshkov flow for elastic materials: the vorticity deposited on the material interface during shock passage is propagated away by the shear waves, whereas for gas dynamics it stays on the interface.

1. Introduction

The instability, caused by the passage of a shock wave, of an interface between two gases was first studied by Richtmyer (1960). His theoretical predictions and numerical calculations were confirmed experimentally by Meshkov (1970), and this type of instability is therefore named the Richtmyer–Meshkov instability. Since this initial work, extensive theoretical, numerical and experimental work has been conducted on the Richtmyer–Meshkov instability. The reader may wish to consult the review article by Rupert (1992) as well as more recent references (e.g. Grove *et al.* 1993; Holmes 1994; Yang, Zhang & Sharp 1994; Zhang & Graham 1998).

A schematic illustration of the Richtmyer–Meshkov flow configuration is shown in figure 1. An incident (left-facing) shock wave impinges on a corrugated material interface, generating transmitted and reflected waves. The type of the reflected wave (shock or rarefaction) is determined by the material parameters; figure 1 shows the case of a reflected shock wave. During the interaction, the material interface is

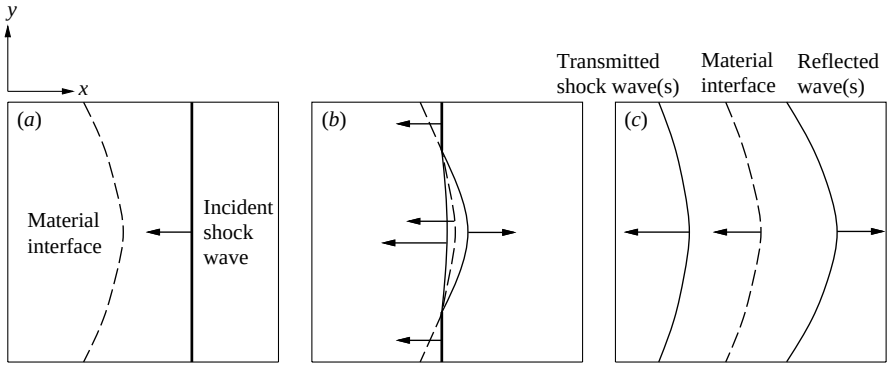

FIGURE 1. An illustration of the Richtmyer–Meshkov flow configuration: (*a*) the incident shock wave and material interface before interaction; (*b*) the interaction between the incident shock and the interface; (*c*) waves emerging after interaction.

accelerated by the incident shock wave. This acceleration can cause the corrugations in the interface to grow in amplitude in an unstable fashion.

In this paper, which is based on the PhD dissertation of J.N.P. (Nam 2001), we study the behaviour of elastic materials, such as metals, in Richtmyer–Meshkov flow. (As we will see, the term 'instability' is not appropriate for elastic materials, so we use the word 'flow'.) In contrast to a gas, an elastic material resists shear strain. Emerging from the interaction of the shock wave with the material interface are transmitted and reflected waves in shear modes, as well as longitudinal modes, which leads to a significant change in the subsequent evolution of the material interface. The tensor nature of strain requires that the principles of solid mechanics be carried over to the analysis of the Richtmyer–Meshkov flow.

Just as Richtmyer did in his pioneering work on the Richtmyer–Meshkov instability for gas dynamics, we start by studying the small-amplitude limit. Our approach is based on Richtmyer's analysis for the case of a reflected shock wave, but it also draws from the refinements of this analysis introduced by Yang *et al.* (1994). In making the transition from gas dynamics to elasticity, we have organized the analysis in a systematic way that facilitates application to general systems of conservation laws.

Concerning related interface instability problems for elastic materials, studies have already been conducted of Kelvin–Helmholtz and Rayleigh–Taylor instability. Adams (1995) investigated the instability of a nearly flat contact surface between two compressible isotropic elastic materials sliding past each other, with a constant coefficient of kinetic friction, and derived the dispersion relation. The interface is stabilized when the velocity jump reaches a threshold set by the shear wave speeds. Plohr & Sharp (1998) considered the acceleration of a nearly flat incompressible elastic plate and solved a linear initial/boundary-value problem to obtain analytic formulae for the solutions. The solutions show that irregularities with sufficiently short wavelengths are stabilized, with the cutoff being related to the plate thickness and to the ratio of the accelerating pressure difference to the shear modulus.

Shear stiffness has a similar effect in Richtmyer–Meshkov flow: according to our simulations, the amplitude remains bounded, oscillating around an asymptotic value, rather than growing linearly with time, as it does for gases; i.e. there is no instability. Moreover, the frequency of the oscillation increases with the shear stiffness of the materials.

An outline of the present paper is as follows. In § 2, we adopt a formulation of the governing equations for elasticity as a system of conservation laws together with a thermoelastic equation of state. A conservative formulation (Plohr & Sharp 1988; Trangenstein & Colella 1991; Plohr & Sharp 1992), as opposed to a conventional incremental formulation, in which the stress evolves according to a differential equation, is essential in the present context where material interface and shock jump conditions must be formulated for two-dimensional configurations of discontinuous solutions. In § 3, we construct the solution to the uniaxial flow problem in which a flat shock impinges normally on a flat material interface. This Riemann-problem solution serves as the background flow about which the Richtmyer–Meshkov flow is a perturbation. In § 4, we linearize the partial differential equations, along with the material interface and shock jump conditions, around the background solution, and we perform some preparatory analysis of the linearized equations in § 5. These equations also come into play in § 6 when formulating the initial conditions for the perturbed flow problem, which amounts to a linearized shock polar problem. In § 7, we describe our numerical scheme. To obtain accurate numerical solutions of the linearized equations, we implement front tracking of the transmitted and reflected waves as well as the material interface, using characteristic tracing to provide coupling from the interior grid points to the fronts. We present the results of numerical simulations using our code in § 8, and discuss the results in § 9.

2. Governing equations

The dynamical equations for an elastic material consist of a system of conservation laws along with corresponding jump conditions for discontinuous solutions and constitutive equations specifying the elastic material response. In this section, we review these equations.

2.1. *Conservation laws*

The partial differential equations governing an elastic material in the Eulerian frame can be written in first-order conservative form (Plohr & Sharp 1988, 1992; Trangenstein & Colella 1991; Wagner 1996). These conservation laws involve, as field variables, the deformation gradient tensor, the velocity vector and a thermodynamic variable, which together characterize the state of the material; and they represent the physical principles of material continuity, conservation of momentum and conservation of energy.

To formulate the Eulerian material continuity equation, we first recall the corresponding equation in the Lagrangian frame (see, e.g. Dafermos 2000). A reference configuration (for instance, the undeformed configuration) is chosen and each point of the body is labelled by its material coordinates X^α, $\alpha = 1, 2, 3$, in this configuration. The motion of the body is described by a time-dependent map ϕ^i specifying the spatial coordinates x^i, $i = 1, 2, 3$, of each material point X^α at time t:

$$x^i = \phi^i(\boldsymbol{X}, t). \tag{2.1}$$

In terms of ϕ^i, the spatial velocity of the particle X^α is the time derivative $V^i := \dot{\phi}^i$, and the deformation of a small neighbourhood of X^α is characterized by the derivative $F^i{}_\alpha := \phi^i{}_{:\alpha}$, which is called the deformation gradient tensor. (The overdot denotes the t-derivative with X^α held fixed, and the semicolon signals differentiation with respect to the indicated variable.) By equating mixed second partial derivatives of ϕ^i,

we obtain the conditions

$$\dot{F}^i{}_\alpha - V^i{}_{;\alpha} = 0, \tag{2.2}$$

$$\epsilon^{\alpha\beta\gamma} F^i{}_{\beta;\gamma} = 0, \tag{2.3}$$

which guarantee that V^i and $F^i{}_\alpha$ are derivatives of a continuous map ϕ^i. The curl-free condition (2.3) is a consequence of (2.2) if it holds at the initial time, so we refer to the dynamical equation (2.2) as the Lagrangian material continuity equation.

The Eulerian material continuity equation derives from the inverse of the relationship (2.1), written

$$X^\alpha = \psi^\alpha(\boldsymbol{x}, t). \tag{2.4}$$

The derivative $g^\alpha{}_i := \psi^\alpha{}_{;i}$, called the inverse deformation gradient tensor, is the inverse of $F^i{}_\alpha$, regarded as a function of x^i rather than X^α. Taking the time derivative of the identity $X^\alpha \equiv \psi^\alpha(\boldsymbol{\phi}(\boldsymbol{X}, t), t)$, we find that $\psi^\alpha{}_{;t} = -g^\alpha{}_k v^k$, where $v^i(\boldsymbol{x}, t) := V^i(\boldsymbol{\phi}(\boldsymbol{x}, t), t)$. Equating the mixed second derivatives of ψ^α yields the material continuity equation and the curl-free condition in Eulerian coordinates (Trangenstein & Colella 1991):

$$\left(g^\alpha{}_i\right)_{;t} + \left(g^\alpha{}_j v^j\right)_{;i} = 0, \tag{2.5}$$

$$\epsilon^{ijk} g^\alpha{}_{j;k} = 0. \tag{2.6}$$

As in the Lagrangian case, these conditions guarantee that $g^\alpha{}_i$ and v^i derive from a continuous map ψ^i, and the curl-free condition is an initial-value constraint.

The mass density of the material is $\rho(\boldsymbol{x}, t) = \rho_0(\boldsymbol{\psi}(\boldsymbol{x}, t)) J(\boldsymbol{x}, t)^{-1}$, where $J = (\det \boldsymbol{g})^{-1}$ is the Jacobian and $\rho_0(\boldsymbol{X})$ is the mass per unit reference volume at material position X^α. Equations (2.5)–(2.6) imply the conservation of mass equation,

$$\rho_{;t} + (\rho v^j)_{;j} = 0. \tag{2.7}$$

To simplify matters, we consider only homogeneous materials; in particular, we assume that ρ_0 is constant throughout each material.

Along with the material continuity equations, the conservation of momentum and energy equations hold (see e.g. Dafermos 2000):

$$(\rho v^i)_{;t} + (\rho v^i v^j - \sigma^{ij})_{;j} = 0, \tag{2.8}$$

$$(\rho e)_{;t} + (\rho e v^j - v_i \sigma^{ij})_{;j} = 0. \tag{2.9}$$

Here σ^{ij} is the Cauchy stress tensor, $e = v_k v^k/2 + \varepsilon$ is the specific total energy, and ε is the specific internal energy. (We neglect body forces and heat flow.)

Equations (2.5), (2.8) and (2.9) represent conservation laws for the conserved quantities $g^\alpha{}_i$, ρv^i and ρe, assuming that the stress tensor σ^{ij} can be expressed in terms of these quantities. The constitutive relationship that so expresses the stress tensor is discussed in § 2.2.

2.2. *Equation of state*

To complete the governing system of conservation laws, we must specify how the stress tensor σ^{ij} relates to the conserved quantities. We adopt a thermoelastic constitutive equation satisfying the axioms of locality, entropy production and material frame indifference (see, e.g. Marsden & Hughes 1983). Such a constitutive equation amounts to an equation of state,

$$\varepsilon = \tilde{\varepsilon}(\mathbf{C}, \eta), \tag{2.10}$$

relating the specific internal energy ε to the right Cauchy–Green strain tensor $\boldsymbol{C} = \boldsymbol{F}^T\boldsymbol{F}$ and the specific entropy η, which determines the Cauchy stress σ^{ij} and the temperature θ through the formulae

$$\sigma^{ij} = 2\rho F^i{}_\alpha \frac{\partial \tilde{\varepsilon}}{\partial C_{\alpha\beta}} F^j{}_\beta, \tag{2.11}$$

$$\theta = \frac{\partial \tilde{\varepsilon}}{\partial \eta}. \tag{2.12}$$

For modelling elastic solids, we assume that ε is the sum of two terms, the volumetric (or 'hydrodynamic') energy and the shear energy. The volumetric energy ε_h accounts for the response of the material to changes in volume; it depends on $\boldsymbol{C}$ solely through the specific volume $\tau = 1/\rho = J/\rho_0$, where $J^2 = \det \boldsymbol{C}$. The shear energy, on the other hand, accounts for the response to shear strain. To measure the shear strain, we define the volume-preserving part of the right Cauchy–Green tensor (Simo & Hughes 1998), $\tilde{\boldsymbol{C}} = J^{-2/3}\boldsymbol{C}$, and the elastic shear distortion, ϵ, given by

$$\epsilon^2 = \tfrac{1}{2}(\operatorname{tr} \tilde{\boldsymbol{C}} - 3). \tag{2.13}$$

Because $\det \tilde{\boldsymbol{C}} = 1$, the tensor $\tilde{\boldsymbol{C}}$ and therefore ϵ are unaffected by volume change; moreover, ϵ reduces to the usual measure of shear strain (the norm of the deviator of the symmetric part of the displacement gradient) in the small-strain limit.

Specifically, we follow Walter *et al.* (1999) in adopting the equation of state

$$\varepsilon = \tilde{\varepsilon}_h(\tau, \eta) + \tau G \epsilon^2, \tag{2.14}$$

where G is the (constant) shear modulus. The resulting Cauchy stress is

$$\sigma^{ij} = -p_{\text{mean}}\delta^{ij} + G(\operatorname{dev} \tilde{b})^{ij}. \tag{2.15}$$

Here, $p_{\text{mean}} = \tilde{p}_h(\tau, \eta) - G\epsilon^2$ is the mean pressure, with

$$\tilde{p}_h(\tau, \eta) = -\frac{\partial \tilde{\varepsilon}_h}{\partial \tau}(\tau, \eta) \tag{2.16}$$

being the hydrodynamic contribution; and $\operatorname{dev} \tilde{\boldsymbol{b}} = \tilde{\boldsymbol{b}} - \operatorname{tr}(\tilde{\boldsymbol{b}})\boldsymbol{I}/3$ is the deviatoric, or trace-free, part of the volume-preserving part of the left Cauchy–Green tensor, $\tilde{\boldsymbol{b}} = J^{-2/3}\boldsymbol{F}\boldsymbol{F}^T$. In § A.1, we give explicit formulae for ϵ^2 and the components of $\operatorname{dev} \tilde{\boldsymbol{b}}$ in terms of the components of $\boldsymbol{g}$ for the case of plane strain that is relevant for the present paper.

The hydrodynamic part of the equation of state remains to be specified. In subsequent calculations, it proves convenient to replace the entropy by an alternative thermodynamic variable. We shall use the hydrodynamic pressure $p = \tilde{p}_h(\tau, \eta)$. One advantage of this choice is that an incomplete form (Menikoff & Plohr 1989) of the hydrodynamic equation of state suffices to close the system of equations. We denote the solution of the relation $p = \tilde{p}_h(\tau, \eta)$ by $\eta = \hat{\eta}_h(\tau, p)$ and define

$$\hat{\varepsilon}_h(\tau, p) = \tilde{\varepsilon}_h(\tau, \hat{\eta}_h(\tau, p)). \tag{2.17}$$

Thus the incomplete forms of formulae (2.14) and (2.15) are

$$\varepsilon = \hat{\varepsilon}_h(\tau, p) + \tau G \epsilon^2, \tag{2.18}$$

$$\sigma^{ij} = -p_{\text{mean}}\delta^{ij} + G(\operatorname{dev} \tilde{b})^{ij} \quad \text{with} \quad p_{\text{mean}} = p - G\epsilon^2. \tag{2.19}$$

Then, as a concrete model for the response of a solid to hydrodynamic pressure, we adopt a stiffened polytropic equation of state (see, e.g. Menikoff & Plohr 1989):

$$\hat{\varepsilon}_h(\tau, p) = \frac{p + (\Gamma + 1)p_\infty}{\Gamma}\tau, \tag{2.20}$$

where Γ and p_∞ are material constants. Recalling the definition of the Grüneisen coefficient, we calculate that it is the constant Γ:

$$\Gamma = \tau \left.\frac{\partial p}{\partial \varepsilon_h}\right|_\tau. \tag{2.21}$$

Similarly, the bulk modulus is

$$K := -\tau \left.\frac{\partial p}{\partial \tau}\right|_\eta = -\tau\left(\left.\frac{\partial p}{\partial \tau}\right|_{\varepsilon_h} - p\left.\frac{\partial p}{\partial \varepsilon_h}\right|_\tau\right) = (\Gamma + 1)(p + p_\infty), \tag{2.22}$$

so that the material constant p_∞ has the significance that $K_0 := (\Gamma + 1)p_\infty$ is the bulk modulus at zero pressure.

2.3. *Quasi-linear form*

The continuity equation (2.5), the momentum equation (2.8), and the energy equation (2.9) are in conservative, or divergence, form. To perform a characteristic analysis and linearisation of this system, we first transform the conservation laws into quasi-linear form. The particular quasi-linear form employed depends on the choice of flow variables. We choose these variables to be the inverse deformation gradient components $g^\alpha{}_i$, the velocity components v^i, and the hydrodynamic pressure p.

The continuity equation (2.5) implies that

$$\left(g^\alpha{}_i\right)_{;t} + v^j g^\alpha{}_{j;i} + g^\alpha{}_j v^j{}_{;i} = 0. \tag{2.23}$$

By the curl-free condition (2.6), the second term is $v^j g^\alpha{}_{i;j}$, so that the first two terms constitute a convective derivative of $g^\alpha{}_i$. That is, using the notation $\dot{a} = a_{;t} + v^j a_{;j}$ for the convective derivative, the continuity equation (2.5) takes the quasi-linear form

$$\dot{g}^\alpha{}_i + g^\alpha{}_j v^j{}_{;i} = 0. \tag{2.24}$$

In the standard manner (see e.g. Gurtin 1981), the quasi-linear forms of the equations for the velocity components are derived by expanding the momentum equation (2.8) and using the mass equation (2.7). The result is

$$\dot{v}^i - \tau \sigma^{ij}{}_{;j} = 0. \tag{2.25}$$

Viewing σ^{ij} as a function of $g^\alpha{}_i$ and p, we find that

$$\dot{v}^i - \tau \left.\frac{\partial \sigma^{ij}}{\partial g^\gamma{}_\ell}\right|_p g^\gamma{}_{\ell;j} - \tau \left.\frac{\partial \sigma^{ij}}{\partial p}\right|_{g^\gamma{}_\ell} p_{;j} = 0. \tag{2.26}$$

Explicit formulae for the stress derivatives appearing in (2.26), specialized to the case of uniaxial deformation that is relevant to this paper, are given in § A.3.

From the energy equation (2.9), we obtain a quasi-linear form of the equation for the hydrodynamic pressure, as follows. Standard manipulations (see, e.g. Gurtin 1981) involving the mass and momentum equations reduce the energy equation to

$$\dot{\varepsilon} - \tau \sigma^{ij} v_{i;j} = 0. \tag{2.27}$$

On the other hand, by the thermoelastic formulae (2.11) and (2.12) for σ^{ij} and θ,

$$\dot{\varepsilon} = \theta\dot{\eta} + \operatorname{tr}\left[\tfrac{1}{2}\tau \boldsymbol{F}^{-1}\boldsymbol{\sigma}(\boldsymbol{F}^{T})^{-1}\dot{\boldsymbol{C}}\right] = \theta\dot{\eta} - \tau \operatorname{tr}[\boldsymbol{\sigma}\boldsymbol{g}^{-1}\dot{\boldsymbol{g}}]. \tag{2.28}$$

Therefore, by (2.24), $\dot{\varepsilon} = \theta\dot{\eta} + \tau\sigma^{ij}v_{i;j}$. Comparing this result to (2.27), we see that the energy equation amounts to $\dot{\eta} = 0$. As $p = \tilde{p}_h(\tau, \eta)$, this means that $\dot{p} = -\rho K\dot{\tau}$, where K is the bulk modulus (2.22). Using the conservation of mass equation, written in the form $\dot{\tau} = \tau v^{j}{}_{;j}$, we arrive at the equation

$$\dot{p} + K v^{j}{}_{;j} = 0. \tag{2.29}$$

for the pressure.

Equations (2.24), (2.26) and (2.29) constitute the quasi-linear form of the equations for the flow variables $g^{\alpha}{}_{i}$, v^{i} and p.

2.4. *Shock conditions*

A solution of a nonlinear system of conservation laws generally develops jump discontinuities, even if its initial data are smooth; and to be compatible with the integral form of the conservation laws, a jump discontinuity must satisfy the Rankine–Hugoniot conditions (see, e.g. Smoller 1994). Solutions of the Rankine–Hugoniot conditions for the conservation laws (2.5), (2.8) and (2.9) for elasticity represent shock waves in either the longitudinal or shear modes.

To specify the Rankine–Hugoniot conditions, consider a point x_*^j on a propagating surface of discontinuity. We use the following notation: n_j denotes the surface normal at this point; s denotes its speed in this normal direction; Q_+ (respectively, Q_-) denotes the limiting value of a quantity Q as $x^j \to x_*^j$ with $n_j(x^j - x_*^j)$ kept positive (respectively, negative); and $\Delta Q := Q_+ - Q_-$ and $\langle Q\rangle := (Q_- + Q_+)/2$. Then the Rankine–Hugoniot conditions for (2.5), (2.8) and (2.9) are

$$-s\Delta g^{\alpha}{}_{i} + \Delta(g^{\alpha}{}_{j}\, v^{j})n_i = 0, \tag{2.30}$$

$$-s\Delta(\rho v^{i}) + \Delta(\rho v^{i}v^{j} - \sigma^{ij})n_j = 0, \tag{2.31}$$

$$-s\Delta(\rho e) + \Delta\left(\rho e v^{j} - v_i\sigma^{ij}\right)n_j = 0. \tag{2.32}$$

2.5. *Material interface conditions*

A material interface is a boundary separating two different materials. The appropriate model for the behaviour of a material interface depends on the problem of interest (welded materials, a lubricated interface, etc.). In the present paper, we assume that: (i) no separation and no penetration of the materials occurs at the material interface; and (ii) no friction resists the relative tangential motion of the materials.

Assumption (i) means that the normal velocity is continuous across the material interface:

$$n_j v_-^j = n_j v_+^j. \tag{2.33}$$

The common value of the normal velocity at the interface is the speed at which the material interface moves normal to itself. The tangential velocity, however, can be discontinuous.

Another quantity that is continuous across the material interface is the traction $\sigma^{ij}n_j$, as follows from (2.31) when combined with the jump condition corresponding to (2.7), namely, $-s\Delta\rho + \Delta(\rho v^{j})n_j = 0$. Assumption (ii) means that the tangential

components of the traction, in fact, vanish. Thus, the traction conditions are

$$n_i \sigma_-^{ij} n_j = n_i \sigma_+^{ij} n_j, \tag{2.34}$$

$$\epsilon_{k\ell m} n^\ell \sigma_-^{mj} n_j = 0 = \epsilon_{k\ell m} n^\ell \sigma_+^{mj} n_j. \tag{2.35}$$

This assumption of no friction at the interface is just one of many possible tangential traction assumptions. We adopt it because it leads to weak shear waves. We expect that the results obtained under this assumption hold more generally. Indeed, shear waves are the key to stabilizing Richtmyer–Meshkov flow, and even weak shear waves effect this stabilization.

2.6. *Vector formulation*

In the present paper, we apply the foregoing governing equations to Richtmyer–Meshkov flow. We choose the coordinate frame such that the incident shock wave is a plane wave in the x^1-direction and the material interface is a small perturbation of the (x^2, x^3)-plane. As we shall see in § 5.1, the linearized equations have coefficients that are independent of x^2 and x^3. Consequently, we may use Fourier analysis in (x^2, x^3) to write any solution as the linear superposition of Fourier modes. Also, because of the covariance of the governing equations under rotations, a Fourier mode with wavenumber $k = (k_2, k_3)$ is obtained by rotation from the Fourier mode with wavenumber $(|k|, 0)$. In other words, without loss of generality, we may assume that the solution is independent of x^3.

Therefore, for the remainder of the paper, we restrict our attention to plane strain flows, in which there is no motion in the $z = x^3$ direction and there is no variation in the motion along this direction. In effect, the flow is two-dimensional, and we occasionally use the notation $x = x^1$ and $y = x^2$. Knowing that $g^3{}_1 = g^3{}_2 = 0 = g^1{}_3 = g^2{}_3$, $g^3{}_3 = 1$ and $v^3 = 0$, we omit these components from consideration. The governing equations for the remaining flow variables can be summarized in a compact vector notation.

We define the conserved quantity vector to be

$$\boldsymbol{W} = \begin{bmatrix} g^1{}_1 & g^1{}_2 & g^2{}_1 & g^2{}_2 & \rho v^1 & \rho v^2 & \rho e \end{bmatrix}^T \tag{2.36}$$

and the state vector to be

$$\boldsymbol{U} = \begin{bmatrix} g^1{}_1 & g^1{}_2 & g^2{}_1 & g^2{}_2 & v^1 & v^2 & p \end{bmatrix}^T. \tag{2.37}$$

Then

$$\boldsymbol{W} = \boldsymbol{H}(\boldsymbol{U}) := [U_1 \quad U_2 \quad U_3 \quad U_4 \quad \rho U_5 \quad \rho U_6 \quad \rho e]^T, \tag{2.38}$$

where $\rho = \rho_0(U_1 U_4 - U_2 U_3)$, $e = \varepsilon_{\text{kinetic}} + \varepsilon$, $\varepsilon_{\text{kinetic}} = [(U_5)^2 + (U_6)^2]/2$, and ε is specified in terms of U_1, U_2, U_3, U_4 and U_7 by the incomplete form of the equation of state (2.18). Similarly, the conservation laws (2.5), (2.8) and (2.9) take the form

$$\boldsymbol{H}(\boldsymbol{U})_{;t} + \boldsymbol{F}(\boldsymbol{U})_{;x} + \boldsymbol{G}(\boldsymbol{U})_{;y} = 0, \tag{2.39}$$

with

$$\boldsymbol{F}(\boldsymbol{U}) := \begin{bmatrix} U_1 U_5 + U_2 U_6 \\ 0 \\ U_3 U_5 + U_4 U_6 \\ 0 \\ \rho (U_5)^2 - \sigma^{11} \\ \rho U_6 U_5 - \sigma^{21} \\ \rho e U_5 - U_5 \sigma^{11} - U_6 \sigma^{21} \end{bmatrix}, \quad \boldsymbol{G}(\boldsymbol{U}) := \begin{bmatrix} 0 \\ U_1 U_5 + U_2 U_6 \\ 0 \\ U_3 U_5 + U_4 U_6 \\ \rho U_5 U_6 - \sigma^{12} \\ \rho (U_6)^2 - \sigma^{22} \\ \rho e U_6 - U_5 \sigma^{12} - U_6 \sigma^{22} \end{bmatrix} \tag{2.40}$$

being the fluxes in the x- and y-directions, respectively, and σ^{ij} being given in terms of U_1, U_2, U_3, U_4 and U_7 by (2.19). In these terms, the Rankine–Hugoniot conditions (2.30), (2.31) and (2.32) are

$$-s\Delta \boldsymbol{H}(\boldsymbol{U}) + \Delta \boldsymbol{F}(\boldsymbol{U})\, n_1 + \Delta \boldsymbol{G}(\boldsymbol{U})\, n_2 = 0. \tag{2.41}$$

Likewise in this notation, the quasi-linear equations (2.24), (2.26) and (2.29) take the form

$$\boldsymbol{U}_{,t} + \boldsymbol{C}(\boldsymbol{U})\, \boldsymbol{U}_{,x} + \boldsymbol{D}(\boldsymbol{U})\, \boldsymbol{U}_{,y} = 0, \tag{2.42}$$

where the coefficient matrices $\boldsymbol{C}(\boldsymbol{U})$ and $\boldsymbol{D}(\boldsymbol{U})$ are readily identified. (See § A.4 for these matrices evaluated in a uniaxial state.)

3. Background solution

In this section, we construct a solution of the governing equations that represents the normal interaction of a plane shock wave with a flat material interface. This solution serves as the background for the Richtmyer–Meshkov flow.

We consider two half-spaces, $x^1 < 0$ and $x^1 > 0$, filled with two different solid materials. The flat interface $x^1 = 0$ between the materials is taken to be frictionless. The background flow arises when a plane shock wave, incident from within the material in $x^1 > 0$ and propagating in the negative x^1-direction, impinges on the material interface. At the moment of collision of the incident shock wave with the interface, the flow conditions are homogeneous in each half-space $x^1 < 0$ and $x^1 > 0$; they therefore constitute the initial conditions of a Riemann initial-value problem. The solution of this Riemann problem contains a transmitted wave, which is a longitudinal shock wave, and a reflected wave, which is either a shock or a rarefaction wave of the longitudinal family, along with an accelerated material interface.

The type of the reflected wave that emerges from the interaction of the incident shock wave with the material interface is influenced primarily by the nature of the two materials and sometimes (in the case of anomalous reflection) by the strength of the incident shock wave. In the present work, we concentrate on the case when the reflected wave is a shock wave. (We are preparing a separate paper in which we treat reflected rarefaction waves.) For the material model that we have chosen, this case occurs when a shock wave in a material with lower longitudinal acoustic impedance is incident on an interface with a material with higher impedance.

3.1. *Uniaxial shock conditions*

The background solution is uniaxial, with all motion and all flow variation being in the $x = x^1$ direction. Therefore the only non-zero components of the inverse deformation gradient, velocity and shock normal are $\bar{g}^1{}_1 = \bar{J}^{-1}$, $\bar{g}^2{}_2 = 1 = \bar{g}^3{}_3$, $\bar{v}^1 =: \bar{v}$ and $\bar{n}_1 = 1$. One consequence is that only the $\alpha = 1$, $i = 1$ component of (2.30) is non-trivial: $-\bar{s}\Delta\left(\bar{J}^{-1}\right) + \Delta\left(\bar{J}^{-1}\bar{v}\right) = 0$. As the shock is assumed to be propagating in a homogeneous material, ρ_0 is a constant, and multiplying this jump condition by ρ_0 yields

$$-\bar{s}\Delta\bar{\rho} + \Delta\left(\bar{\rho}\bar{v}\right) = 0, \tag{3.1}$$

which is the jump condition corresponding to conservation of mass (2.7). Another consequence of uniaxiality is the reduction of (2.31) and (2.32) to

$$-\bar{s}\Delta(\bar{\rho}\bar{v}) + \Delta[\bar{\rho}(\bar{v})^2 - \bar{\sigma}^{11}] = 0, \tag{3.2}$$

$$\Delta\bar{\sigma}^{12} = 0 = \Delta\bar{\sigma}^{13}, \tag{3.3}$$

$$-\bar{s}\Delta(\bar{\rho}\bar{e}) + \Delta(\bar{\rho}\bar{e}\bar{v} - \bar{v}\bar{\sigma}^{11}) = 0, \tag{3.4}$$

where $\bar{e} = (\bar{v})^2/2 + \bar{\varepsilon}$. Notice that (3.3) is satisfied automatically because $\bar{\sigma}^{12}$ and $\bar{\sigma}^{13}$ vanish for a uniaxial deformation.

Equations (3.1), (3.2) and (3.4) are the same as the Rankine–Hugoniot conditions for gas dynamics, except that the pressure has been replaced by $-\bar{\sigma}^{11}$. The usual manipulations (see, e.g. Menikoff & Plohr 1989) reduce these equations to the following:

$$\bar{\rho}_-(\bar{v}_- - \bar{s}) = \mp\bar{m} = \bar{\rho}_+(\bar{v}_+ - \bar{s}), \tag{3.5}$$

$$\mp\bar{m}\Delta\bar{v} - \Delta\bar{\sigma}^{11} = 0, \tag{3.6}$$

$$\Delta\bar{\varepsilon} - \langle\bar{\sigma}^{11}\rangle\Delta\bar{\tau} = 0, \tag{3.7}$$

where the mass flux $\bar{m} > 0$ and the upper (respectively, lower) sign is for a right-facing (respectively, left-facing) shock wave. In particular,

$$\bar{v}_- \pm \bar{m}\bar{\tau}_- = \bar{s} = \bar{v}_+ \pm \bar{m}\bar{\tau}_+ \quad \text{with} \quad \bar{m} = \sqrt{\frac{\Delta\bar{\sigma}^{11}}{\Delta\bar{\tau}}} \tag{3.8}$$

and

$$\Delta\bar{v} = \mp\,\mathrm{sgn}(\Delta\bar{\tau})\sqrt{\Delta\bar{\sigma}^{11}\Delta\bar{\tau}}. \tag{3.9}$$

3.2. *Shock curves*

Consider the problem of solving the Rankine–Hugoniot conditions for the state variables behind a shock wave (labelled by b) in terms of the fixed state ahead (labelled by a) and a single parameter. For the equation of state that we have adopted, $\bar{\varepsilon}$ and $\bar{\sigma}^{11}$ are given by equations (2.18)–(2.20), specialized as in § A.2. In particular, $\bar{p}_b$ appears linearly in the Hugoniot relation (3.7), which may therefore be solved to express $\bar{p}_b$ in terms of $\bar{\tau}_b$ and the state ahead of the shock wave:

$$\bar{p}_b = -p_\infty + (\bar{p}_a + p_\infty)\frac{\langle\bar{\tau}\rangle - \frac{1}{2}(\Gamma+1)\Delta\bar{\tau}}{\langle\bar{\tau}\rangle + \frac{1}{2}(\Gamma+1)\Delta\bar{\tau}} + \Gamma G\frac{\langle\overline{(\mathrm{dev}\,\tilde{b})^{11}}\rangle\Delta\bar{\tau} - \langle\bar{\tau}\rangle\Delta(\bar{\epsilon}^2)}{\langle\bar{\tau}\rangle + \frac{1}{2}(\Gamma+1)\Delta\bar{\tau}}, \tag{3.10}$$

when $\Gamma/(\Gamma+2) < \bar{\tau}_b/\bar{\tau}_a \leqslant 1$; here, we use the notation $\Delta Q := Q_b - Q_a$. Substitution of this expression into the formulae for other quantities, for example, (A 14) for $\bar{\sigma}_b^{11}$ and (3.9) for $\bar{v}_b$, yields their values along the shock curve. Thus we obtain a parameterization of the shock curve by $\bar{\tau}_b$.

Examples of such shock curves, drawn in the $(\bar{v}_b, -\bar{\sigma}_b^{11})$-plane, are shown in figure 2. The incident curve I parameterizes left-facing shock waves in aluminium (Al) with state A ahead (i.e. on the left-hand sides) of the waves. State A is defined by $\bar{\tau}_A = \tau_{0,\mathrm{Al}}$, $\bar{p}_A = 0$, and $\bar{v}_A = 0$. One such shock wave has state B behind it, where $\bar{\tau}_B = 0.85\,\tau_{0,\mathrm{Al}}$. The reflected shock curve R parameterizes right-facing shock waves in aluminium with state B ahead (i.e. on the right-hand sides) of the waves. One such shock wave has state C behind it, where $\bar{\tau}_C \approx 0.78\,\tau_{0,\mathrm{Al}}$. Additionally, the transmitted curve T parameterizes left-facing shock waves in tantalum (Ta) with state A' ahead ($\bar{\tau}_{A'} = \tau_{0,\mathrm{Ta}}$, $\bar{p}_{A'} = 0$, and $\bar{v}_{A'} = 0$), and one such shock wave has state C' behind it, where $\bar{\tau}_{C'} \approx 0.89\,\tau_{0,\mathrm{Ta}}$. Because $\bar{v}_{C'} = \bar{v}_C$ and $\bar{\sigma}_{C'}^{11} = \bar{\sigma}_C^{11}$ (cf. (2.33) and (2.34)), these three shock waves fit together to form a solution of a Riemann problem corresponding to the interaction of the incident shock wave with a tantalum–aluminium interface to generate the reflected and transmitted shock waves, as indicated in the space–time diagram, figure 3.

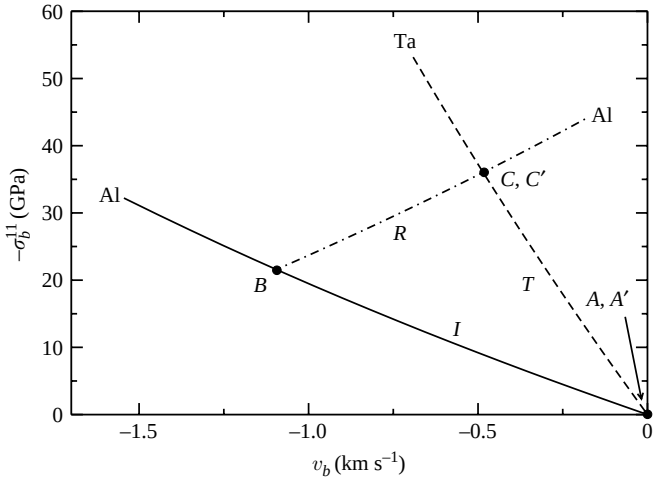

FIGURE 2. Shock curves drawn in the $(\bar{v}_b, -\bar{\sigma}_b^{11})$-plane.

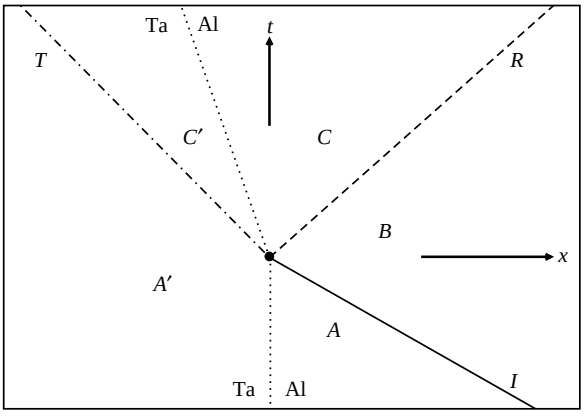

FIGURE 3. Wave interaction diagram, depicted in space–time.

3.3. *Incident shock wave*

The background wave pattern for the Richtmyer–Meshkov problem arises when a shock wave is incident on a material interface. Without loss of generality, we assume that the shock wave is incident from the right, and that it arrives at the interface at $x = 0$ when $t = 0$. An example was discussed in the preceding section (see figure 3): a left-facing shock wave propagates through aluminium and strikes a tantalum–aluminium interface; this incident shock wave connects the ambient state of aluminium, labelled A, to a shocked state labelled B.

Equation (3.10) expresses the pressure behind the shock wave in terms of the specific volume behind the wave together with the entire state ahead of the wave. Rather than parameterizing the incident wave by the volume, however, we choose to parameterize by the incident shock speed $\bar{s}_I > 0$. Substituting (3.10) into (A 14) to obtain $\bar{\sigma}_b^{11}$ and using the result in (3.8) expresses $\bar{s}_I$ in terms of $\bar{\tau}_b$; inverting this relation (e.g. with a numerical equation solver) gives the parameterization of the incident shock wave by $\bar{s}_I$.

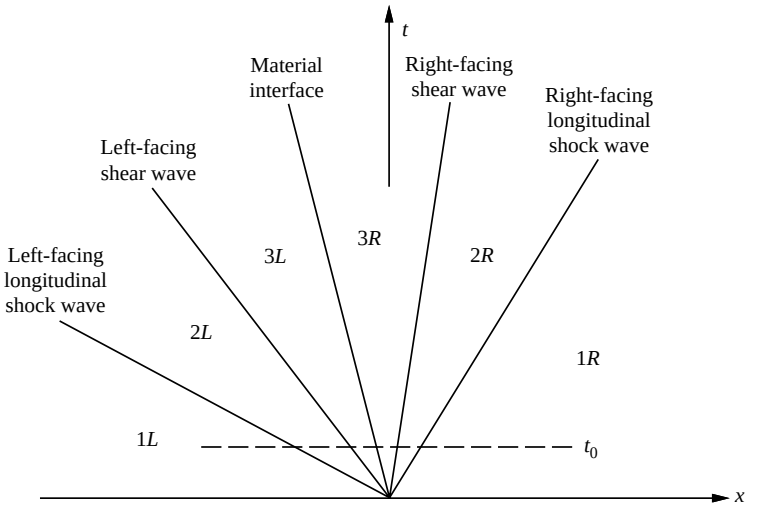

FIGURE 4. Background waves and sectors in the (x, t)-plane.

3.4. *Riemann solution*

When the incident shock wave arrives at the material interface, the state of the solid materials is homogeneous to the left, as well as to the right, of the shock wave. Such a situation constitutes a Riemann initial-value problem for the conservation laws (2.5), (2.8) and (2.9), as restricted to this one-dimensional setting.

As we shall see presently, a uniaxial elastic Riemann problem can be solved using only left- and right-facing longitudinal waves along with a material interface. No shear waves are required; i.e. the shear waves have zero strength. For the situation considered in the present paper, the longitudinal waves are shock waves. Therefore the waves in the Riemann solution divide space–time into sectors, which are labelled in the manner indicated in figure 4. (The right- and left-facing shear waves are acoustic waves, with speeds being the shear characteristic speeds.) The waves themselves are indicated by the subscripts ℓL, sL, i, sR and ℓR, respectively.

Consider whether a wave pattern containing only uniaxial longitudinal shock waves and a material interface can satisfy the boundary conditions at the material interface. There is a one-parameter family of left-facing longitudinal shock waves with $\bar{\boldsymbol{U}}_{2L}$ as the state behind the wave and $\bar{\boldsymbol{U}}_{1L}$ fixed as the state ahead, and there is a second one-parameter family of right-facing longitudinal shock waves with $\bar{\boldsymbol{U}}_{2R}$ as the state behind the wave and $\bar{\boldsymbol{U}}_{1R}$ fixed as the state ahead. Also, because there are no shear waves, $\bar{\boldsymbol{U}}_{3L} = \bar{\boldsymbol{U}}_{2L}$ and $\bar{\boldsymbol{U}}_{3R} = \bar{\boldsymbol{U}}_{2R}$. On the other hand, the normal velocity boundary condition (2.33) requires that $\bar{v}_{3L} = \bar{v}_{3R}$; the normal traction boundary condition (2.34) requires that $\bar{\sigma}^{11}_{3L} = \bar{\sigma}^{11}_{3R}$; and the vanishing of the tangential traction (2.35) is satisfied automatically by uniaxiality. Thus the boundary conditions at the material interface are satisfied if the two shock parameters are chosen so that two conditions hold, namely, continuity of normal velocity and traction.

Recall that (3.10) and (A 14) give the normal traction $\bar{\sigma}^{11}_{2L}$ behind the left-facing longitudinal shock wave in terms of $\bar{\tau}_{2L}$ and the state $\bar{\boldsymbol{U}}_{1L}$ ahead of the wave. Inverting this relationship (e.g. numerically) determines $\bar{\tau}_{2L}$ in terms of $\bar{\sigma}^{11}_{2L}$ and $\bar{\boldsymbol{U}}_{1L}$, which gives the parameterization of $\bar{\boldsymbol{U}}_{2L}$ by $\bar{\sigma}^{11}_{2L}$. Similarly, $\bar{\boldsymbol{U}}_{2R}$ is parameterized by $\bar{\sigma}^{11}_{2R}$.

Let $\bar{v}_*$ and $\bar{\sigma}^{11}_*$ denote the common values of normal velocity and traction in the sectors $2L$, $3L$, $3R$ and $2R$. Then the two boundary conditions at the material interface

amount to (3.6) applied to the left- and right-facing longitudinal shock waves:

$$\bar{m}_{\ell L}(\bar{v}_* - \bar{v}_{1L}) = \bar{\sigma}_*^{11} - \bar{\sigma}_{1L}^{11}, \tag{3.11}$$

$$-\bar{m}_{\ell R}(\bar{v}_* - \bar{v}_{1R}) = \bar{\sigma}_*^{11} - \bar{\sigma}_{1R}^{11}, \tag{3.12}$$

where $\bar{m}_{\ell L}$ and $\bar{m}_{\ell R}$ denote the mass fluxes through the respective shock waves. Solving these equations for $\bar{v}_*$ and $\bar{\sigma}_*^{11}$ yields the equations

$$\bar{\sigma}_*^{11} = \frac{-\bar{v}_{1L} + \bar{v}_{1R} + \bar{m}_{\ell L}^{-1}\bar{\sigma}_{1L}^{11} + \bar{m}_{\ell R}^{-1}\bar{\sigma}_{1R}^{11}}{\bar{m}_{\ell L}^{-1} + \bar{m}_{\ell R}^{-1}}, \tag{3.13}$$

$$\bar{v}_* = \frac{-\bar{\sigma}_{1L}^{11} + \bar{\sigma}_{1R}^{11} + \bar{m}_{\ell L}\bar{v}_{1L} + \bar{m}_{\ell R}\bar{v}_{1R}}{\bar{m}_{\ell L} + \bar{m}_{\ell R}}. \tag{3.14}$$

Equation (3.13) is a fixed-point equation for $\bar{\sigma}_*^{11}$. Once this equation is solved, all requisite quantities in the Riemann solution can be determined. For example, $\bar{v}_*$ may be calculated from (3.14).

Remark. For the numerical simulations, it is convenient to change to a moving coordinate frame in which the material interface is stationary. To this end, we simply subtract $\bar{v}_*$ from each of the velocities.

4. Linearization

In this section, the system of the governing equations derived in § 2 is linearized around the background solution constructed in § 3. For the case of a reflected shock wave that we consider in this paper, the background solution comprises two longitudinal shock waves and a material interface whose trajectories divide space–time domain into sectors in which the background solution is constant. It proves useful to consider the trajectories of the two (zero-strength, i.e. acoustic) shear waves in the background solution as further dividing space–time. In a space–time sector so defined, the constant state vector of the background solution is denoted $\bar{\boldsymbol{U}}$, and the perturbed solution is written $\boldsymbol{U} = \bar{\boldsymbol{U}} + \tilde{\boldsymbol{U}}$.

Consider one of the shock waves, one of the shear waves, or the material interface in the background solution. The states on its left- and right-hand sides are denoted $\bar{\boldsymbol{U}}_-$ and $\bar{\boldsymbol{U}}_+$. Its trajectory has the form $x = \bar{s}t$, so that it propagates in the $\bar{\boldsymbol{n}} = (1, 0)$ direction with speed $\bar{s}$. The quantities $\bar{\boldsymbol{U}}_-$, $\bar{\boldsymbol{U}}_+$ and $\bar{s}$ are related by internal boundary conditions, such as the Rankine–Hugoniot conditions (2.41) or the material interface conditions (2.33)–(2.35). A perturbation of this background wave has trajectory of the form $x = \bar{s}t + \tilde{a}(y, t)$, so that it propagates in the $\boldsymbol{n} = (1, -\tilde{a}_{,y})/N$ direction with speed $s = (\bar{s} + \tilde{a}_{,t})/N$, where the normalization factor $N = [1 + (\tilde{a}_{,y})^2]^{1/2}$ is equal to 1 to first order in the perturbation amplitude. We write $s = \bar{s} + \tilde{s}$ and $n_i = \bar{n}_i + \tilde{n}_i$, where $\bar{\boldsymbol{n}} = (1, 0)$. Then, to first order in the perturbation, $\tilde{s} = \tilde{a}_{,t}$, $\tilde{n}_1$ vanishes, and $\tilde{n}_2 = -\tilde{a}_{,y}$.

Thus the perturbation is described by $\tilde{\boldsymbol{U}}$ for each of four sectors and by $\tilde{a}$, or equivalently $\tilde{s}$ and $\tilde{n}_2$, for each of five waves. These perturbed quantities are subject to the following linear equations.

4.1. *Linearization of the partial differential equations*

The background solution is piecewise constant in space–time. Therefore $\bar{\boldsymbol{U}}$ trivially satisfies the quasi-linear system of partial differential equations, equation (2.42), away from from the jump discontinuities in the background solution. The linearization of

this system about $\bar{\boldsymbol{U}}$ is the system

$$\tilde{\boldsymbol{U}}_{;t} + \boldsymbol{C}(\bar{\boldsymbol{U}})\tilde{\boldsymbol{U}}_{;x} + \boldsymbol{D}(\bar{\boldsymbol{U}})\tilde{\boldsymbol{U}}_{;y} = 0, \tag{4.1}$$

which is to be solved for the perturbation $\tilde{\boldsymbol{U}}$. Once $\tilde{\boldsymbol{U}}$ is found, $\boldsymbol{U} = \bar{\boldsymbol{U}} + \tilde{\boldsymbol{U}}$ approximately solves system (2.42).

4.2. *Linearization of the shock conditions*

The linearized Rankine–Hugoniot conditions provide internal boundary conditions at the background shock waves. These conditions relate the state perturbations $\tilde{\boldsymbol{U}}_-$ and $\tilde{\boldsymbol{U}}_+$ in adjacent space–time sectors to the speed and direction perturbation for the shock wave, $\tilde{s}$ and $\tilde{n}_2$.

Consider one of the two longitudinal shock waves in the background solution. The quantities $\bar{\boldsymbol{U}}_-$, $\bar{\boldsymbol{U}}_+$ and $\bar{s}$ are related by the Rankine–Hugoniot conditions (2.41) for $\boldsymbol{n} = \bar{\boldsymbol{n}}$, which reduce to

$$-\bar{s}\Delta\boldsymbol{H}(\bar{\boldsymbol{U}}) + \Delta\boldsymbol{F}(\bar{\boldsymbol{U}}) = 0. \tag{4.2}$$

Therefore the linearization of Rankine–Hugoniot conditions (2.41) about the background solution is

$$-\bar{s}\Delta[\boldsymbol{H}'(\bar{\boldsymbol{U}})\tilde{\boldsymbol{U}}] - \Delta\boldsymbol{H}(\bar{\boldsymbol{U}})\,\tilde{s} + \Delta[\boldsymbol{F}'(\bar{\boldsymbol{U}})\tilde{\boldsymbol{U}}] + \Delta\boldsymbol{G}(\bar{\boldsymbol{U}})\,\tilde{n}_2 = 0. \tag{4.3}$$

If $\tilde{\boldsymbol{U}}_-$, $\tilde{\boldsymbol{U}}_+$ and $\tilde{s}$ satisfy this equation for some $\tilde{n}_2$, then $\boldsymbol{U}_- = \bar{\boldsymbol{U}}_- + \tilde{\boldsymbol{U}}_-$, $\boldsymbol{U}_+ = \bar{\boldsymbol{U}}_+ + \tilde{\boldsymbol{U}}_+$ and $s = \bar{s} + \tilde{s}$ approximately satisfy the Rankine–Hugoniot conditions (2.41) for $\boldsymbol{n} = \bar{\boldsymbol{n}} + (0, \tilde{n}_2)$. Formulae for the quantities appearing as coefficients in (4.3) are developed in §§A.3 and A.5.

4.3. *Linearization of the shear wave conditions*

In the background solution, the shear waves are absent, so that the background states adjacent at each shear wave coincide: $\bar{\boldsymbol{U}}_- = \bar{\boldsymbol{U}}_+ =: \bar{\boldsymbol{U}}$. Therefore, in the linearized Rankine–Hugoniot condition (4.3), the second and fourth terms vanish, and this condition reduces to

$$[-\bar{s}\,\boldsymbol{H}'(\bar{\boldsymbol{U}}) + \boldsymbol{F}'(\bar{\boldsymbol{U}})]\Delta\tilde{\boldsymbol{U}} = 0. \tag{4.4}$$

This equation requires $\Delta\tilde{\boldsymbol{U}}$ to be a right eigenvector corresponding to the eigenvalue $\bar{s}$ of $\boldsymbol{H}'(\bar{\boldsymbol{U}})^{-1}\boldsymbol{F}'(\bar{\boldsymbol{U}})$. Using the formulae for $\boldsymbol{H}'(\bar{\boldsymbol{U}})$ and $\boldsymbol{F}'(\bar{\boldsymbol{U}})$ in §A.5, it is easily verified directly that

$$\begin{bmatrix} 0 & 0 & 1 & 0 & 0 & \pm\bar{c}_s & 0 \end{bmatrix}^T \tag{4.5}$$

is a right eigenvector with eigenvalue $\bar{s} = \bar{v} \pm \bar{c}_s$, where

$$\bar{c}_s := \left(-\frac{1}{\bar{\rho}} \overline{\left.\frac{\partial\sigma^{21}}{\partial g_1^2}\right|_p} \right)^{1/2} = \left(\frac{G[1 + O(\bar{J} - 1)]}{\bar{\rho}} \right)^{1/2} \tag{4.6}$$

is the shear sound speed. Therefore the linearized conditions at the right-facing (respectively, left-facing) shear wave are

$$\tilde{g}^1_{-1} = \tilde{g}^1_{+1}, \qquad \tilde{g}^1_{-2} = \tilde{g}^1_{+2}, \qquad \tilde{g}^2_{-2} = \tilde{g}^2_{+2}, \tag{4.7}$$

$$\tilde{v}^1_- = \tilde{v}^1_+, \qquad \tilde{p}_- = \tilde{p}_+, \tag{4.8}$$

$$\tilde{v}^2_+ - \tilde{v}^2_- = \pm\bar{c}_s \left[\tilde{g}^2_{+1} - \tilde{g}^2_{-1}\right]. \tag{4.9}$$

Also, $\tilde{s}$ can be determined from the formula $s = v \pm c_s$, but in practice, we simply dispense with the variables $\tilde{s}$, $\tilde{n}_2$ and $\tilde{a}$ associated with shear waves.

4.4. *Linearization of the material interface conditions*

The linearization of the conditions at the background material interface provides a relation between the state perturbations $\tilde{\boldsymbol{U}}_-$ and $\tilde{\boldsymbol{U}}_+$ on its left- and right-hand sides and the direction perturbation $\tilde{n}_2$.

As $\tilde{n}^x$ vanishes to first order in the perturbation amplitude, the normal speed of the material interface, namely the common value of $n_j v^j$, is $\bar{v} + \tilde{v}^1$ to first order. The background satisfies $\bar{v}_- = \bar{v}_+$, so that the linearisation of the condition (2.33) of normal velocity continuity, and the identification of the common value of the normal velocity as the speed of the interface, reduces to

$$\tilde{v}^1_- = \tilde{s} = \tilde{v}^1_+. \tag{4.10}$$

Similarly, the traction components are $\sigma^{ij} n_j = \bar{\sigma}^{i1} + \tilde{\sigma}^{i1} + \bar{\sigma}^{i2}\tilde{n}_2$ to first order. Because $\bar{\sigma}^{12}_- = 0 = \bar{\sigma}^{12}_+$, we find that, to first order in the perturbation, the normal traction is

$$n_i \sigma^{ij} n_j = \bar{\sigma}^{11} + \tilde{\sigma}^{11}, \tag{4.11}$$

and the only non-zero tangential traction component is

$$\epsilon_{3\ell m} n^\ell \sigma^{mj} n_j = \tilde{\sigma}^{12} + (\bar{\sigma}^{22} - \bar{\sigma}^{11})\tilde{n}_2. \tag{4.12}$$

Therefore, with the notation $\bar{\sigma}^{11}_- = \bar{\sigma}^{11}_+ =: \bar{\sigma}^{11}$, the linearisations of the traction conditions (2.34) and (2.35) are

$$\tilde{\sigma}^{11}_- = \tilde{\sigma}^{11}_+, \tag{4.13}$$

$$\tilde{\sigma}^{12}_- + (\bar{\sigma}^{22}_- - \bar{\sigma}^{11})\tilde{n}_2 = 0 = \tilde{\sigma}^{12}_+ + (\bar{\sigma}^{22}_+ - \bar{\sigma}^{11})\tilde{n}_2. \tag{4.14}$$

Expressed in terms of components of the perturbation of the state vector $\tilde{\boldsymbol{U}}$ for a uniaxial background solution $\bar{\boldsymbol{U}}$, the linearized stress components are

$$\tilde{\sigma}^{11} = \overline{\left.\frac{\partial \sigma^{11}}{\partial g^1{}_1}\right|_p} \tilde{g}^1{}_1 + \overline{\left.\frac{\partial \sigma^{11}}{\partial g^2{}_2}\right|_p} \tilde{g}^2{}_2 + \overline{\left.\frac{\partial \sigma^{11}}{\partial p}\right|_{g^{\gamma}{}_k}} \tilde{p}, \tag{4.15}$$

$$\tilde{\sigma}^{12} = \overline{\left.\frac{\partial \sigma^{12}}{\partial g^1{}_2}\right|_p} \tilde{g}^1{}_2 + \overline{\left.\frac{\partial \sigma^{12}}{\partial g^2{}_1}\right|_p} \tilde{g}^2{}_1, \tag{4.16}$$

$$\tilde{\sigma}^{22} = \overline{\left.\frac{\partial \sigma^{22}}{\partial g^1{}_1}\right|_p} \tilde{g}^1{}_1 + \overline{\left.\frac{\partial \sigma^{22}}{\partial g^2{}_2}\right|_p} \tilde{g}^2{}_2 + \overline{\left.\frac{\partial \sigma^{22}}{\partial p}\right|_{g^{\gamma}{}_k}} \tilde{p}, \tag{4.17}$$

as shown in § A.3. Substituting these equations and using the explicit formulae for the coefficients that appear, which are also derived in § A.3, we obtain the linearized traction conditions.

5. Analysis

In this section, we perform some preliminary analysis on the linearized governing equations that facilitate their solution.

5.1. *Fourier analysis*

The linearized governing equations for the perturbation, developed in § 4, have coefficients that depend on t and x, but are independent of y. Therefore we can reduce the dimensionality of the system of partial differential equations using Fourier analysis in the y-direction: any perturbation solution is a linear superposition of Fourier modes. Without loss of generality, we assume in this work that the initial

perturbation of the material interface takes the form $x = \hat{a}_0 \cos(ky)$, where $k > 0$. Then the solution contains only two modes of wavelength $2\pi/k$.

Mathematically, it is easy to account for both of these modes by writing the perturbation of the state vector in the form $\tilde{\boldsymbol{U}}(x, y, t) = \hat{\boldsymbol{U}}(x, t)\exp(iky)$, where $\hat{\boldsymbol{U}}$ takes complex values, and similarly for the other perturbation variables. Complex variables are inconvenient for numerical calculations, however, being less efficient in storage space and in speed than real variables. To avoid them, we take advantage of the symmetry of the equations of elasticity and the background solution under the reflection $y \mapsto -y$.

Define

$$\tilde{\boldsymbol{U}}_e := \begin{bmatrix} \tilde{g}^1{}_1 & \tilde{g}^2{}_2 & \tilde{v}^1 & \tilde{p} \end{bmatrix}, \tag{5.1}$$

$$\tilde{\boldsymbol{U}}_o := \begin{bmatrix} \tilde{g}^1{}_2 & \tilde{g}^2{}_1 & \tilde{v}^2 \end{bmatrix}. \tag{5.2}$$

As may be verified by examining (A 25) and (A 26), the linearized system (4.1) takes the form

$$(\tilde{\boldsymbol{U}}_e)_{,t} + \boldsymbol{C}(\bar{\boldsymbol{U}})_{ee}(\tilde{\boldsymbol{U}}_e)_{,x} + \boldsymbol{D}(\bar{\boldsymbol{U}})_{eo}(\tilde{\boldsymbol{U}}_o)_{,y} = 0, \tag{5.3}$$

$$(\tilde{\boldsymbol{U}}_o)_{,t} + \boldsymbol{C}(\bar{\boldsymbol{U}})_{oo}(\tilde{\boldsymbol{U}}_o)_{,x} + \boldsymbol{D}(\bar{\boldsymbol{U}})_{oe}(\tilde{\boldsymbol{U}}_e)_{,y} = 0. \tag{5.4}$$

In other words, the matrix blocks $\boldsymbol{C}(\bar{\boldsymbol{U}})_{eo}$, $\boldsymbol{C}(\bar{\boldsymbol{U}})_{oe}$, $\boldsymbol{D}(\bar{\boldsymbol{U}})_{ee}$ and $\boldsymbol{D}(\bar{\boldsymbol{U}})_{oo}$ are zero. Therefore, the system is preserved under the transformation $y \mapsto -y$, $\tilde{\boldsymbol{U}}_e \mapsto \tilde{\boldsymbol{U}}_e$ and $\tilde{\boldsymbol{U}}_o \mapsto -\tilde{\boldsymbol{U}}_o$. In particular, if we define

$$\tilde{\boldsymbol{U}}_e(x, y, t) := \hat{\boldsymbol{U}}_e(x, t)\cos(ky), \tag{5.5}$$

$$\tilde{\boldsymbol{U}}_o(x, y, t) := \hat{\boldsymbol{U}}_o(x, t)\sin(ky), \tag{5.6}$$

then

$$(\hat{\boldsymbol{U}}_e)_{,t} + \boldsymbol{C}(\bar{\boldsymbol{U}})_{ee}(\hat{\boldsymbol{U}}_e)_{,x} + k\boldsymbol{D}(\bar{\boldsymbol{U}})_{eo}\hat{\boldsymbol{U}}_o = 0, \tag{5.7}$$

$$(\hat{\boldsymbol{U}}_o)_{,t} + \boldsymbol{C}(\bar{\boldsymbol{U}})_{oo}(\hat{\boldsymbol{U}}_o)_{,x} - k\boldsymbol{D}(\bar{\boldsymbol{U}})_{oe}\hat{\boldsymbol{U}}_e = 0. \tag{5.8}$$

Take note of the change of sign in the last equation. Equivalently, if $\boldsymbol{A}(\bar{\boldsymbol{U}}) := \boldsymbol{C}(\bar{\boldsymbol{U}})$ and $\boldsymbol{B}(\bar{\boldsymbol{U}})$ is the same as $\boldsymbol{D}(\bar{\boldsymbol{U}})$ except that its second, third and sixth rows are opposite in sign (i.e. $\boldsymbol{B}(\bar{\boldsymbol{U}})_{oe} = -\boldsymbol{D}(\bar{\boldsymbol{U}})_{oe}$), then

$$\hat{\boldsymbol{U}}_{,t} + \boldsymbol{A}(\bar{\boldsymbol{U}})\hat{\boldsymbol{U}}_{,x} + k\boldsymbol{B}(\bar{\boldsymbol{U}})\hat{\boldsymbol{U}} = 0. \tag{5.9}$$

Similarly, if $\tilde{s} \mapsto \tilde{s}$ and $\tilde{n}_2 \mapsto -\tilde{n}_2$ under y-reflection, then each component of the linearized shock conditions (4.3), of the linearized shear wave conditions (4.7)–(4.9), and of the linearized material interface conditions (4.10), (4.13) and (4.14) is preserved. Therefore, if we define

$$\tilde{s}(y, t) := \hat{s}(t)\cos(ky), \tag{5.10}$$

$$\tilde{n}_2(y, t) := \hat{n}_2(t)\sin(ky), \tag{5.11}$$

(i.e. if we define $\tilde{a}(y, t) := \hat{a}(t)\cos(ky)$ and identify $\hat{s} = \hat{a}_{,t}$ and $\hat{n}_2 = k\hat{a}$), then the foregoing internal boundary conditions take the same form for the Fourier transformed variables. For instance, (4.3) becomes

$$-\bar{s}\Delta[\boldsymbol{H}'(\bar{\boldsymbol{U}})\hat{\boldsymbol{U}}] - \Delta\boldsymbol{H}(\bar{\boldsymbol{U}})\hat{s} + \Delta[\boldsymbol{F}'(\bar{\boldsymbol{U}})\hat{\boldsymbol{U}}] + \Delta\boldsymbol{G}(\bar{\boldsymbol{U}})\hat{n}_2 = 0. \tag{5.12}$$

5.2. *Characteristic analysis*

The eigenvalues of the coefficient matrix $\boldsymbol{A}(\bar{\boldsymbol{U}}) = \boldsymbol{C}(\bar{\boldsymbol{U}})$ appearing in (5.9) and given explicitly in (A 25) are the characteristic velocities. These eigenvalues are easily

computed and have the familiar form

$$\bar{v}, \qquad \bar{v} \pm \bar{c}_s, \qquad \bar{v} \pm \bar{c}_\ell, \tag{5.13}$$

where $\bar{c}_s$ is the shear sound speed, given by (4.6), and

$$\bar{c}_\ell := \left[-\frac{1}{\bar{\rho}} \left(\bar{K} \overline{\frac{\partial \sigma^{11}}{\partial p}\bigg|_{g^{\gamma}{}_k}} + \bar{J}^{-1} \overline{\frac{\partial \sigma^{11}}{\partial g^1{}_1}\bigg|_p} \right) \right]^{1/2} = \left(\frac{\bar{K} + \frac{4}{3} G[1 + O(\bar{J} - 1)]}{\bar{\rho}} \right)^{1/2} \tag{5.14}$$

is the longitudinal sound speed. The eigenvalue $\bar{v}$ has multiplicity three, reflecting that η, $g^1{}_2$ and $g^2{}_2$ are Riemann invariants for this eigenvalue (see the left eigenvectors $\boldsymbol{\ell}_3$, $\boldsymbol{\ell}_4$ and $\boldsymbol{\ell}_5$ below). We label the eigenvalues as follows:

$$\lambda_1 := \bar{v} - \bar{c}_\ell, \qquad \lambda_2 := \bar{v} - \bar{c}_s, \tag{5.15}$$

$$\lambda_3 := \bar{v}, \qquad \lambda_4 := \bar{v}, \qquad \lambda_5 := \bar{v}, \tag{5.16}$$

$$\lambda_6 := \bar{v} + \bar{c}_s, \qquad \lambda_7 := \bar{v} + \bar{c}_\ell. \tag{5.17}$$

Left eigenvectors corresponding to these eigenvalues are

$$\boldsymbol{\ell}_1 := \left[-\overline{\partial \sigma^{11}/\partial g^1{}_1|_p} \quad 0 \quad 0 \quad -\overline{\partial \sigma^{11}/\partial g^2{}_2|_p} \quad -\bar{\rho}\bar{c}_\ell \quad 0 \quad -\overline{\partial \sigma^{11}/\partial p|_{g^{\gamma}{}_k}} \right], \tag{5.18}$$

$$\boldsymbol{\ell}_2 := \left[0 \quad -\overline{\partial \sigma^{12}/\partial g^1{}_2|_p} \quad -\overline{\partial \sigma^{12}/\partial g^2{}_1|_p} \quad 0 \quad 0 \quad -\bar{\rho}\bar{c}_s \quad 0 \right], \tag{5.19}$$

$$\boldsymbol{\ell}_3 := \left[-\bar{J}\bar{K} \quad 0 \quad 0 \quad -\bar{K} \quad 0 \quad 0 \quad 1 \right], \tag{5.20}$$

$$\boldsymbol{\ell}_4 := \left[0 \quad 1 \quad 0 \quad 0 \quad 0 \quad 0 \quad 0 \right], \tag{5.21}$$

$$\boldsymbol{\ell}_5 := \left[0 \quad 0 \quad 0 \quad 1 \quad 0 \quad 0 \quad 0 \right], \tag{5.22}$$

$$\boldsymbol{\ell}_6 := \left[0 \quad -\overline{\partial \sigma^{12}/\partial g^1{}_2|_p} \quad -\overline{\partial \sigma^{12}/\partial g^2{}_1|_p} \quad 0 \quad 0 \quad \bar{\rho}\bar{c}_s \quad 0 \right], \tag{5.23}$$

$$\boldsymbol{\ell}_7 := \left[-\overline{\partial \sigma^{11}/\partial g^1{}_1|_p} \quad 0 \quad 0 \quad -\overline{\partial \sigma^{11}/\partial g^2{}_2|_p} \quad \bar{\rho}\bar{c}_\ell \quad 0 \quad -\overline{\partial \sigma^{11}/\partial p|_{g^{\gamma}{}_k}} \right]. \tag{5.24}$$

6. Initial conditions

To initialize a numerical simulation of a linearized Richtmyer–Meshkov flow, we must specify the initial perturbations of the wave fronts and the states. In this section, we determine these initial conditions. The characteristic analysis of the previous section shows that five waves emerge from the interaction of the incident shock wave and the material interface. In the case considered in the present paper, where the incident shock sweeps through the material with lower impedance first, the reflected waves, as well as the transmitted waves, are shock waves. As mentioned in § 5.1, we assume that the initial perturbation of the material interface takes the form $x = \hat{a}_0 \cos(ky)$, where $k > 0$; all waves that emerge from the interaction have perturbed fronts of a similar sinusoidal form, with the same wavelength and phase. We also make the assumption that $|k\hat{a}_0| \ll 1$, which is basic for the validity of the linearized analysis.

6.1. *Initial amplitudes*

Let us apply the simple geometric argument of Richtmyer (1960) to find the initial amplitude for the perturbation of each front. Figure 5 illustrates the configuration of waves near a point of interaction between the incident shock wave and the material interface. As the flat shock wave interacts with the material interface, which is inclined because of its sinusoidal perturbation, waves emanate from the moving interaction

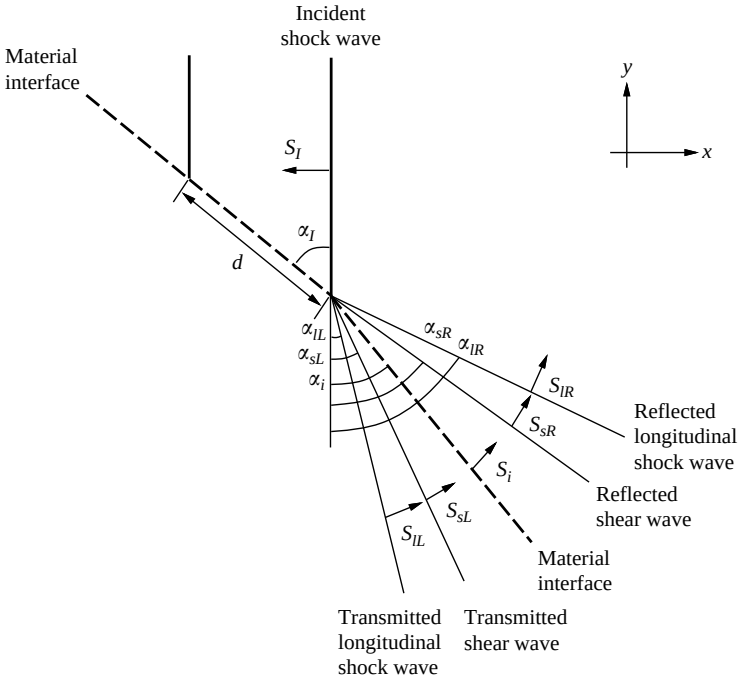

FIGURE 5. Interaction of the incident shock wave and the material interface.

point, or node. The speeds of these waves and their inclination angles are related to the speed of the moving node. In figure 5, the node moves a distance d during a time interval Δt. For definiteness, let us work in a reference frame in which the material interface is stationary before interacting with the shock wave; and let the other waves move normal to themselves at the speeds S_I, $S_{\ell L}$, S_{sL}, S_i, S_{sR} and $S_{\ell R}$, respectively, in the directions indicated in figure 5.

Geometrically, we find the following equalities:

$$d = \frac{S_I \Delta t}{\sin \alpha_I} = \frac{S_\mu \Delta t}{\sin(\alpha_\mu - \alpha_I)}, \tag{6.1}$$

for $\mu = \ell L$, sL, i, sR and ℓR. As $|k\hat{a}_0| \ll 1$, so too is $|k\hat{a}_\mu(0^+)| \ll 1$. Therefore,

$$\frac{S_\mu}{S_I} = \frac{\sin(\alpha_\mu - \alpha_I)}{\sin \alpha_I} \approx \frac{\hat{a}_\mu(0^+)}{\hat{a}_0} - 1, \tag{6.2}$$

where $\hat{a}_\mu(0^+)$ is the initial perturbation amplitude of wave μ in the solution after the interaction.

The wave speeds in figure 5 are related to incident shock speed and the wave speeds occurring in the solution of the background Riemann problem. Indeed, $S_I = \bar{s}_I$, and to first order in the initial perturbation amplitude, $S_\mu \approx \bar{s}_\mu$ for $\mu = \ell L$, sL, i, sR and ℓR. Combining this result with the approximation (6.2), we arrive at the following formula for the initial perturbations amplitude:

$$\hat{a}_\mu(0^+) = \left(1 + \frac{\bar{s}_\mu}{\bar{s}_I}\right) \hat{a}_0. \tag{6.3}$$

In particular, because $\bar{s}_I > 0$ and $\bar{s}_i < 0$, this formula implies that $\hat{a}_i(0^+) < \hat{a}_0$, i.e. the perturbation amplitude of the interface is smaller after the interaction than prior to the interaction.

6.2. *Initial states and speeds*

The initial perturbations of the states provide the initial data for the linearized governing equations. In the background problem, the origin of time $t = 0$ is taken to be the interaction time, and the left and the right states of the Riemann problem constitute the initial data. By contrast, the appropriate choice for the origin of the time for the perturbed problem is ambiguous because the interaction between the incident shock wave and the perturbed material interface takes place over a time interval of non-zero duration. This interaction is intrinsically two-dimensional, whereas the linearized treatment is quasi-one-dimensional. In particular, the linear theory is valid only after this interaction. Therefore, we initiate the numerical simulation of the linearized equations at some positive time $t = t_0 > 0$ rather than at $t = 0$. The results of our calculations prove to be insensitive to the precise value of t_0, so long as it is much smaller than the time scale $1/(k\bar{s}_I)$ of the flow. For definiteness, t_0 is taken to be the time $\hat{a}_0/\bar{s}_I$ required for the incident shock wave to cross (half of) the initially perturbed interface.

Because five background waves emanate from the origin $(0, 0)$ in the (x, t)-plane (see figure 4), spatial regions have opened up between them at $t = t_0$. Therefore, initial states must be specified throughout these regions. These regions correspond to the spatial sectors in figure 5 between the waves that emerge from the moving node. The states in these sectors can be determined by viewing the configuration of waves in figure 5 as a steady two-dimensional solution of the equations of elasticity, as follows.

Consider a solution of the form as shown in figure 5, involving discontinuities along rays emanating from a single point (the node), spatially and temporally constant states in the sectors bounded by the discontinuities, and the node moving at a constant velocity. By choice of reference frame, the node velocity can be chosen to be zero, so that the solution is steady. The states between the waves and the angles of the waves are constrained only by the appropriate Rankine–Hugoniot conditions (2.41) or material interface conditions (2.33), (2.34) and (2.35) that hold at each wave, together with the conditions that the waves meet at the node. Such a solution is the analogue, for elasticity, of a shock–contact interaction solution for gas dynamics obtained through shock polar analysis (see, e.g. Courant & Friedrichs 1976).

When the angle between the incident shock wave and the material interface is small, the solution is a small perturbation of the normal incidence solution, which is the one-dimensional Riemann problem solved in § 3. The linearisations of the Rankine–Hugoniot and material interface conditions about the normal incidence solution are therefore identical to the internal boundary conditions laid out in § 4, namely, (4.3) for each of the two longitudinal shock waves, (4.7)–(4.9) for each of the two shear waves, and (4.10), (4.13) and (4.14) for the material interface. We regard these 31 equations as linear equations for 31 unknown quantities: the seven state perturbation components in each the four sectors between the waves, and the speed perturbations for the two longitudinal shock waves and the material interface. These equations also involve the amplitudes for the longitudinal shock waves and the material interface, but these amplitudes are known from (6.3), which was derived from the conditions that the waves meet at the node.

Some simplification of the linear system occurs. Recall from § 5.1 that the linearized internal boundary conditions are preserved under y-reflection when the variables are

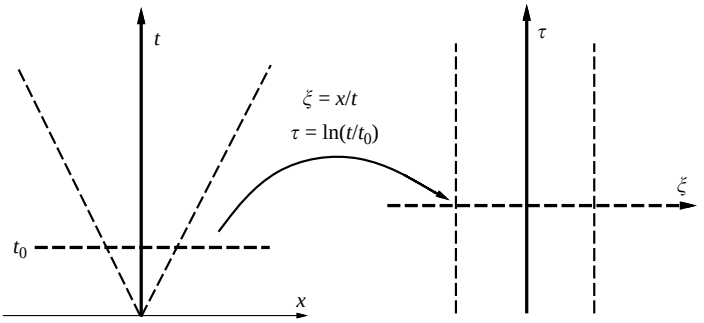

FIGURE 6. Coordinate change from (x, t) to (ξ, τ).

suitably defined as even or odd. Notice also that the inhomogeneous terms in the linear system arise from the $\tilde{n}_2$ terms in (4.3) and (4.14), which couple only to the odd variables. Therefore, the even variables in the solution, namely, $\tilde{g}^1{}_1$, $\tilde{g}^2{}_2$, $\tilde{v}^1$, $\tilde{p}$ and $\tilde{s}$, necessarily vanish.

By solving the linear system, we obtain state perturbations in the four sectors between the waves in figure 5, We assign these states as constant initial data in each of the corresponding regions at $t = t_0$ between the waves in figure 4. Also, the linear system yields initial values for the speed perturbations, and (6.3) gives initial values for the wave amplitudes.

Remark. In his analysis for gas dynamics, Richtmyer (1960) linearizes the well-known shock polar relations to determine the initial conditions. Our equivalent approach reveals the close connection between the construction of initial conditions and the linearized internal boundary conditions.

7. Numerical scheme

In this section we describe the numerical scheme used to solve the linearized governing equations.

7.1. *Coordinate change*

The computation of the solution is to be carried out in the space–time region between the left-facing and right-facing longitudinal shock waves, as indicated in figure 6. Because these waves move apart, the length of the spatial domain increases with time. Therefore, if the spatial grid size Δx were fixed, an increasing number of grid points would be required at successive time steps. To avoid this inconvenient feature, we follow Yang *et al.* (1994) in changing coordinates from (x, t) to (ξ, τ), where $\xi = x/t$ and $\tau = \ln(t/t_0)$. Here the constant t_0, which has units of time, is taken to be small in a sense explained in § 6.2; $t = t_0$ corresponds to $\tau = 0$, which is the beginning of the numerical simulations. This change of coordinates is shown in figure 6. Relative to these new coordinates, the background discontinuous waves, each of which moves at a constant speed, have fixed positions, and thus the regions between waves have fixed lengths.

Upon changing coordinates in this fashion, the system of partial differential equations (5.9) is transformed as follows. Let $\boldsymbol{u}(\xi, \tau) := \hat{\boldsymbol{U}}(x, t)$ stand for the state perturbation regarded as a function of (ξ, τ) rather than (x, t). Then, because $t\partial_x = \partial_\xi$

and $t\partial_t = -\xi\partial_\xi + \partial_\tau$, (5.9) becomes

$$\boldsymbol{u}_{;\tau} + [\boldsymbol{A}(\bar{\boldsymbol{U}}) - \xi\boldsymbol{I}]\boldsymbol{u}_{;\xi} + kt_0\exp(\tau)\boldsymbol{B}(\bar{\boldsymbol{U}})\boldsymbol{u} = 0. \tag{7.1}$$

Notice that the eigenvalues of the coefficient matrix $\boldsymbol{A}(\bar{\boldsymbol{U}})-\xi\boldsymbol{I}$ are $\lambda_k-\xi$, with $\boldsymbol{\ell}_k$ being a corresponding left eigenvector, for $k = 1, \ldots, 7$. For the purpose of discretization, we rewrite (7.1) in the following divergence form:

$$\boldsymbol{u}_{;\tau} + \boldsymbol{f}(\boldsymbol{u}, \xi)_{;\xi} = \boldsymbol{g}(\boldsymbol{u}, \tau), \tag{7.2}$$

where

$$\boldsymbol{f}(\boldsymbol{u}, \xi) := [\boldsymbol{A}(\bar{\boldsymbol{U}}) - \xi\boldsymbol{I}]\boldsymbol{u}, \tag{7.3}$$

$$\boldsymbol{g}(\boldsymbol{u}, \tau) := -[\boldsymbol{I} + kt_0\exp(\tau)\boldsymbol{B}(\bar{\boldsymbol{U}})]\boldsymbol{u}. \tag{7.4}$$

7.2. *Numerical scheme for interior regions*

The solution of the linearized governing equations are approximated by discrete values u_m^n of the state vector at grid points ξ_m and time levels τ^n. The grid spacing $\Delta\xi$ is taken to be uniform, and the time step $\Delta\tau$ is chosen so that the Courant–Friedrichs–Levy condition is satisfied. We use use the two-step Lax–Wendroff scheme (see, e.g. Strikwerda 1989) applied to (7.2):

$$\begin{aligned}\boldsymbol{u}_{m+1/2}^{n+1/2} = {} & \tfrac{1}{2}\left(\boldsymbol{u}_m^n + \boldsymbol{u}_{m+1}^n\right) - \tfrac{1}{2}\frac{\Delta\tau}{\Delta\xi}\left[\boldsymbol{f}\left(\boldsymbol{u}_{m+1}^n, \xi_{m+1}\right) - \boldsymbol{f}\left(\boldsymbol{u}_m^n, \xi_m\right)\right] \\ & + \tfrac{1}{4}\Delta\tau\left[\boldsymbol{g}\left(\boldsymbol{u}_m^n, \tau^n\right) + \boldsymbol{g}\left(\boldsymbol{u}_{m+1}^n, \tau^n\right)\right], \end{aligned} \tag{7.5}$$

$$\begin{aligned}\boldsymbol{u}_m^{n+1} = {} & \boldsymbol{u}_m^n - \frac{\Delta\tau}{\Delta\xi}\left[\boldsymbol{f}\left(\boldsymbol{u}_{m+1/2}^{n+1/2}, \xi_{m+1/2}\right) - \boldsymbol{f}\left(\boldsymbol{u}_{m-1/2}^{n+1/2}, \xi_{m-1/2}\right)\right] \\ & + \tfrac{1}{2}\Delta\tau\left[\boldsymbol{g}\left(\boldsymbol{u}_{m-1/2}^{n+1/2}, \tau^{n+1/2}\right) + \boldsymbol{g}\left(\boldsymbol{u}_{m+1/2}^{n+1/2}, \tau^{n+1/2}\right)\right]. \end{aligned} \tag{7.6}$$

Notice the absence of artificial viscosity terms; the reason for not needing such terms, and indeed the adverse effects of artificial viscosity, are discussed in § 8.1. The scheme is formally second-order accurate.

7.3. *Numerical schemes for internal boundaries*

An internal boundary, or front, is one of the background waves, i.e. a longitudinal shock wave, a shear wave, or the material interface. Because the background solution is generally discontinuous at internal boundaries, the numerical scheme must treat the solution near them in a special manner. In §§ 4.2, 4.3 and 4.4, we derived the linearized Rankine–Hugoniot conditions for the longitudinal shock waves, the eigenvector conditions for the shear waves, and the linearized material interface conditions. In this section, we combine these internal boundary conditions with the method of characteristics and with linear extrapolation to implement a front-tracking scheme.

In addition to the states $\boldsymbol{u}_m^n$ at the interior grid points ξ_m, we associate with each of the five background waves: (a) two states, $\boldsymbol{u}_-^n$ and $\boldsymbol{u}_+^n$, corresponding to the limiting left and right states at the wave; (b) a speed s^n corresponding to the perturbation speed $\hat{s}$; and (c) an amplitude a^n corresponding to the perturbation amplitude $\hat{a}$. According to the type of background wave, these quantities are related by the linearized shock conditions (4.3), the linearized shear wave conditions (4.7)–(4.9), or the linearized material interface conditions (4.10), (4.13) and (4.14). (Recall that $\hat{n}_2 = k\hat{a}$.) In addition,

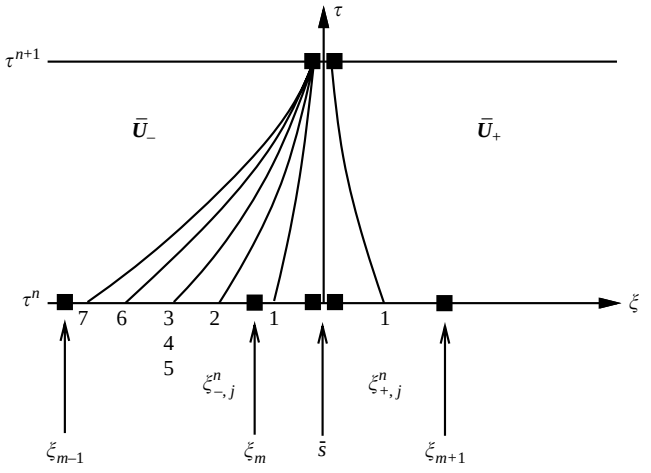

FIGURE 7. Characteristics impinging on a left-facing longitudinal shock wave.

the perturbation amplitude is related to the speed perturbation through the ordinary differential equation $\hat{a}_{;\tau} = t_0 \exp(\tau)\hat{s}$.

Remark. As the linearized shear-wave conditions involve neither the perturbation speed nor the perturbation amplitude, we dispense with these variables for shear waves.

The evolution of the on-front quantities is influenced by, as well as influences, the evolution of the interior states. This coupling is implemented numerically as follows.

7.3.1. *Coupling of the front to the interior*

The interior states close to a front influence the on-front quantities via characteristics that impinge on the front. This influence supplements the internal boundary conditions, which are insufficient in number, by themselves, to determine the evolution of front quantities. We now present the details of the numerical scheme for evolving the left-facing longitudinal shock wave; the schemes for the other background waves are similar.

There are sixteen on-front quantities to be determined: the two states $\boldsymbol{u}_-^{n+1}$ and $\boldsymbol{u}_+^{n+1}$ (each with seven components), the shock speed perturbation s^{n+1}, and the perturbation amplitude a^{n+1}. The linearized shock conditions (5.12) constitute seven equations. Solving the differential equation $\hat{a}_{;\tau} = t_0 \exp(\tau)\hat{s}$ yields one more equation, which we approximate by

$$a^{n+1} = a^n + t_0[\exp(\tau^{n+1}) - \exp(\tau^n)]\tfrac{1}{2}(s^n + s^{n+1}). \tag{7.7}$$

To obtain the remaining eight equations, we employ the method of characteristics. First, we trace the characteristics back from the front to nearby points in the interior. In the case of the left-facing longitudinal shock wave, there are seven characteristics impinging on the left side of the wave and one characteristic impinging on the right side, as shown in figure 7.

More precisely, let $\lambda_{-,j}$ denote the jth eigenvalue, and let $\boldsymbol{\ell}_{-,j}$ denote the corresponding left eigenvector, for the background state $\bar{\boldsymbol{U}}_-$ on the left side of the

background wave. Applying the eigenvectors to (7.1) yields

$$[\partial_\tau + (\lambda_{-,j} - \xi)\partial_\xi]\boldsymbol{\ell}_{-,j}\boldsymbol{u} = -kt_0 \exp(\tau)\boldsymbol{\ell}_{-,j}\boldsymbol{B}(\bar{\boldsymbol{U}}_-)\boldsymbol{u}. \tag{7.8}$$

Let the jth characteristic curve on the left side of the background wave be the solution, denoted $\xi = \bar{\xi}_{-,j}(\tau)$, of the following problem:

$$\frac{\mathrm{d}\xi}{\mathrm{d}\tau} = \lambda_{-,j} - \xi, \qquad \xi = \bar{s} \text{ when } \tau = \tau^{n+1}, \tag{7.9}$$

where $\bar{s}$ denotes the speed of the background wave. Integrating (7.8) along the jth characteristic, we find that

$$\boldsymbol{\ell}_{-,j}[\boldsymbol{u}(\bar{s}, \tau^{n+1}) - \boldsymbol{u}(\bar{\xi}_{-,j}(\tau^n), \tau^n)] = -kt_0\boldsymbol{\ell}_{-,j}\boldsymbol{B}(\bar{\boldsymbol{U}}_-)\int_{\tau^n}^{\tau^{n+1}} \exp(\tau)\,\boldsymbol{u}(\bar{\xi}_{-,j}(\tau), \tau)\,\mathrm{d}\tau. \tag{7.10}$$

We approximate this result as follows:

$$\boldsymbol{\ell}_{-,j}[\boldsymbol{u}_-^{n+1} - \boldsymbol{u}_{-,j}^n] = -kt_0[\exp(\tau^{n+1}) - \exp(\tau^n)] \cdot \boldsymbol{\ell}_{-,j}\boldsymbol{B}(\bar{\boldsymbol{U}}_-)\boldsymbol{u}_{-,j}^n, \tag{7.11}$$

where $\boldsymbol{u}_{-,j}^n$ is obtained by interpolation among the states for time level τ^n at the foot of the characteristic curve,

$$\xi_{-,j}^n := \bar{\xi}_{-,j}(\tau^n) = \exp(\Delta\tau)\bar{s} + [1 - \exp(\Delta\tau)]\lambda_{-,j}. \tag{7.12}$$

Equation (7.10) for $j = 1, \ldots, 7$ constitute seven additional equations for the on-front quantities. One final equation is obtained by an analogous argument concerning the $j = 1$ characteristic on the right side of the background wave. Thus we obtain a complete set of linear equations for the on-front quantities at the left-facing longitudinal shock wave. Similar considerations apply to the right-facing longitudinal shock wave.

For the shear waves, the equations corresponding to the six characteristics impinging on one side and two characteristics impinging on the other side, along with the six linearized internal boundary conditions (4.7)–(4.9), constitute a complete set of equations for the fourteen on-front quantities, $\boldsymbol{u}_-^{n+1}$ and $\boldsymbol{u}_+^{n+1}$.

Similarly, for the material interface, there are five characteristics impinging on each side, and five linearized internal boundary conditions, namely, (4.10), (4.13) and (4.14), which, along with (7.7), completely determine the 16 on-front quantities, $\boldsymbol{u}_-^{n+1}$, $\boldsymbol{u}_+^{n+1}$, a^{n+1} and s^{n+1}.

7.3.2. *Coupling of the interior to the front.*

In § 7.2, we described the scheme (7.5)–(7.6) that is applied to interior states that are sufficiently far from the fronts, in that the three stencil points ξ_{m-1}, ξ_m and ξ_{m+1} lie in the same sector (i.e. the same side of all of the background waves). If one of the stencil points lies on the opposite side of a background wave from the other two, then the interior scheme is modified to account for the influence of the front on the interior.

Consider the particular situation shown in figure 8. Recall that the solution $\boldsymbol{u}$ is generally discontinuous at the background wave as a consequence of the discontinuity in the background solution, even when the initial data for $\boldsymbol{u}$ are smooth. Therefore applying the Lax–Wendroff scheme to the states $\boldsymbol{u}_{m-1}^n$, $\boldsymbol{u}_m^n$ and $\boldsymbol{u}_{m+1}^n$ to obtain $\boldsymbol{u}_m^{n+1}$ would not be a good scheme. To circumvent this problem, we (i) replace $\boldsymbol{u}_{m+1}^n$ by $(\boldsymbol{u}_{m+1}^n)^*$, obtained by linearly extrapolating from from $\boldsymbol{u}_m^n$ at ξ_m and $\boldsymbol{u}_-^n$ at $\bar{s}$ to the position ξ_{m+1} and (ii) apply the Lax–Wendroff scheme to $\boldsymbol{u}_{m-1}^n$, $\boldsymbol{u}_m^n$ and $(\boldsymbol{u}_{m+1}^n)^*$ to

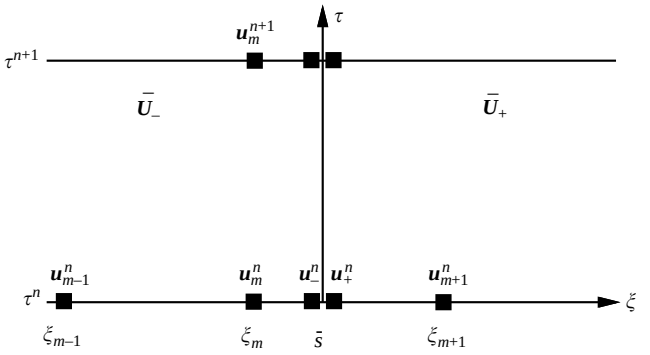

FIGURE 8. Grid configuration near a background wave.

obtain $\boldsymbol{u}_m^{n+1}$. A similar scheme is used when the grid point ξ_{m-1} is separated from ξ_m and ξ_{m+1} by a background wave.

Remark. An alternative to this linear extrapolation scheme is constant extrapolation, in which $(\boldsymbol{u}_{m+1}^n)^*$ is set to $\boldsymbol{u}_-^n$. In our numerical experiments, we have found that constant extrapolation is insufficiently accurate for long time integration; see § 8.1. On the other hand, the linear extrapolation method is prone to spurious oscillations if the spacing between the extrapolation points is too small. Therefore we optimize the spatial grid so that, for each of the five background waves, $\bar{s}$ lies as close as possible to half-way between adjacent grid points. (Here we take advantage of having stationary fronts in (ξ, τ)-coordinates.)

8. Results

In this section, we present some results from our simulations of Richtmyer–Meshkov flow. For the purpose of verifying our numerical algorithm and implementation, we first apply our code to a gas dynamics problem for which there is a published solution. Then we apply the code to some Richtmyer–Meshkov flow problems involving materials with shear stiffness.

8.1. *Gas dynamics*

A Richtmyer–Meshkov flow configuration for polytropic gases can be characterized for dimensionless parameters, as follows. Let L and R indicate the gases on the left- and right-hand sides of the material interface in figure 1 (a), and let R, a and R, b indicate the states of gas R ahead of and behind the incident shock wave. Then the dimensionless parameters are the Grüneisen parameters Γ_L and Γ_R, the density ratio $\bar{\rho}_L/\bar{\rho}_{R,a}$, and the strength of the incident shock wave, measured, for example, by the Mach number $\bar{M}_I = \bar{s}_I/\bar{c}_{R,a}$ or the pressure ratio $\bar{S}_I = (\bar{p}_{R,b} - \bar{p}_{R,a})/\bar{p}_{R,b}$. Following Yang *et al.* (1994), we choose units so that $\bar{\rho}_{R,a} = 1$, the wavenumber is $k = 1$, and the incident shock speed is $\bar{s}_I = 1$.

The gas dynamics test problem is drawn from the paper of Yang *et al.* (1994). The material parameters $\Gamma_L = 0.0935$, $\Gamma_R = 0.4$ and $\bar{\rho}_L/\bar{\rho}_{R,a} = 5.1$ correspond to the heavier gas on the left being sulphur hexafluoride (SF_6) and the lighter gas on the right being air. The incident pressure ratio is $\bar{S}_I = 0.385$, corresponding to a Mach number of $\bar{M}_I = 1.24$. In figure 9, we present a plot of the (normalized) growth rate $\hat{s}_i/\hat{a}_0 = (\hat{a}_i/\hat{a}_0)_{,t}$ of the material interface *vs.* time t as calculated by our code. For

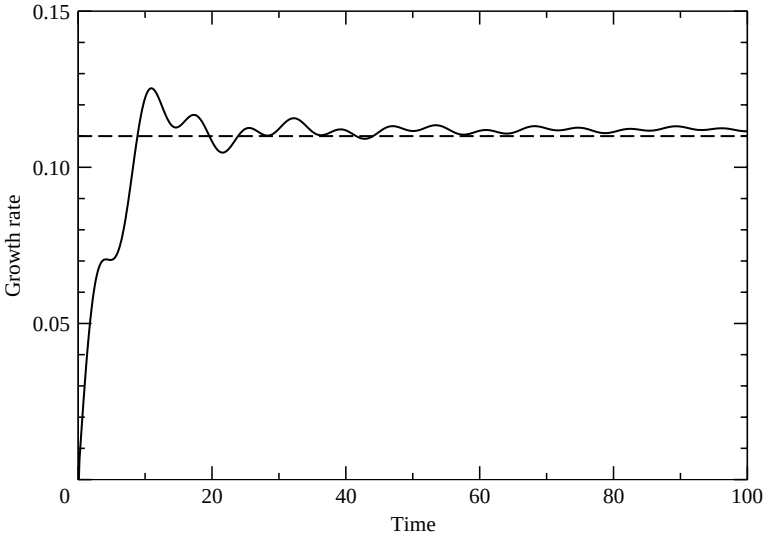

FIGURE 9. Growth rate *vs.* time for the Yang–Zhang–Sharp gas dynamics test problem.

this Richtmyer–Meshkov flow problem involving two gases, the growth rate increases quickly early on, falls for a short time, and then tends toward a positive asymptotic value that roughly (but not exactly) agrees with the prediction of the impulsive model of Richtmyer (1960) (shown as the growth rate value of 0.11 in the figure). In this sense, the material interface between gases is linearly unstable in Richtmyer–Meshkov flow.

Our growth rate results are identical to those of Yang *et al.* (1994) (which are presented in figure 7 of this paper); so too are our results (not shown here) for pressure *vs.* position. This successful comparison gives us confidence that our numerical implementation yields the correct solution for gases. In addition, we performed some numerical experiments to examine how the parameters involved in the numerical scheme affect the results.

For instance, we verified that the solution had converged under mesh refinement (with 459 grid points used for the solution shown in figure 9). We also checked the effect of artificial viscosity. Adding linear artificial viscosity,

$$b\left[\boldsymbol{u}^n_{m+1} - 2\boldsymbol{u}^n_m + \boldsymbol{u}^n_{m-1}\right], \tag{8.1}$$

to the second step, (7.6), of the Lax–Wendroff method, where $b > 0$ is a non-dimensional constant, dampens the spurious oscillations that typically appear, but it also reduces the accuracy of the method to first order. Figure 10 shows how artificial viscosity affects the growth rate: when the integration time is long (the number of time steps is several times the number of grid points), as it is in our simulations, the growth rate computed with artificial viscosity drifts significantly from the correct result. These examples demonstrate the need to avoid artificial viscosity. The Lax–Wendroff method is successful without artificial viscosity because, in a method that tracks all fronts, it is applied only where the solution is smooth. Figure 10 also shows that a similar problem with long time integration occurs if the algorithm for coupling the interior to the front uses constant, rather than linear, extrapolation. These results suggest that the numerical method must be second-order accurate. For this reason, we do not use a TVD scheme (see, e.g. LeVeque 1992) in the interior.

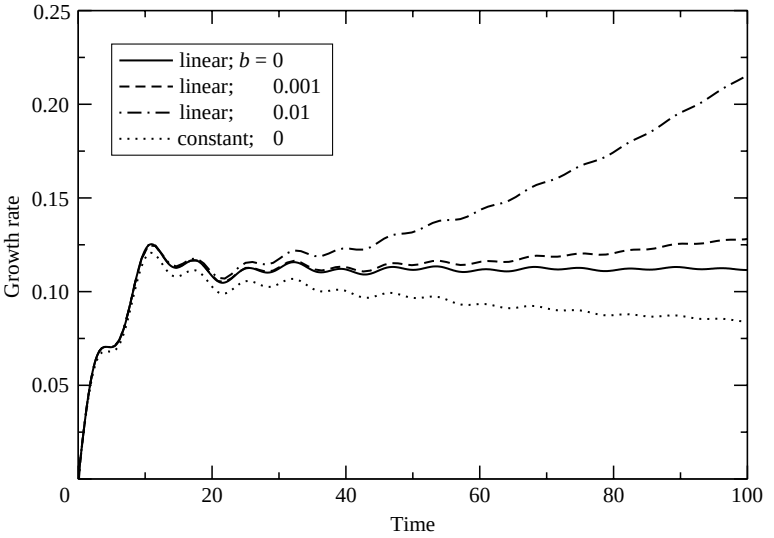

FIGURE 10. Growth rate *vs.* time for the gas dynamics test problem, as calculated with various artificial viscosity coefficients and with constant, instead of linear, extrapolation at the fronts.

8.2. *Elastic materials*

Our model of an elastic material involves two parameters not present for a polytropic gas: the shear modulus G and the bulk modulus $K_0 = (\Gamma + 1)p_\infty$ at zero pressure. The former parameter accounts for shear stiffness, and the latter for the non-zero sound speed at zero pressure. The main focus of this paper is the effect of these parameters on the growth rate of the perturbation amplitude in Richtmyer–Meshkov flow.

As an example of Richtmyer–Meshkov flow involving elastic materials, we take the heavier material on the left to be tantalum and the lighter material on the right to be aluminium. Tantalum is modelled as having $\rho_{0,\mathrm{Ta}} = 16.69\,\mathrm{g\,cm^{-3}}$, $\Gamma_{\mathrm{Ta}} = 1.67$, $G_{\mathrm{Ta}} = 69.0\,\mathrm{GPa}$, and $K_{0,\mathrm{Ta}} = 194.\mathrm{GPa}$; aluminium is modelled as having $\rho_{0,\mathrm{Al}} = 2.707\,\mathrm{g\,cm^{-3}}$, $\Gamma_{\mathrm{Al}} = 1.97$, $G_{\mathrm{Al}} = 27.1\,\mathrm{GPa}$, and $K_{0,\mathrm{Al}} = 78.5\,\mathrm{GPa}$. For this and other test problems in this section, we take $\bar{p}_{R,a} = 10^{-4}\,\mathrm{GPa}$ and $k = 1\,\mathrm{mm^{-1}}$. The unit of time in all graphs is 1 μs.

To aid in exploring the effect of shear stiffness, we introduce a dimensionless interpolation parameter κ between 0 and 1 and replace the shear moduli of tantalum and aluminium by κG_{Ta} and κG_{Al}, respectively. We report on six runs corresponding to the values $\kappa = 0.001$, 0.01, 0.05, 0.2, 0.6 and 1.0. In these runs, we keep the Mach number of the incident shock wave fixed at $\bar{M}_I = 1.076$. (When $\kappa = 1$, the speed of the incident shock wave is $\bar{s}_I = 7.0\,\mathrm{km\,s^{-1}}$, the particle velocity behind it is $0.70\,\mathrm{km\,s^{-1}}$, and the pressure behind it is 9.7 GPa.)

First we take $\kappa = 0.001$, so that the shear modulus is small. The (normalized) growth rate $\hat{s}_i/\hat{a}_0 = (\hat{a}_i/\hat{a}_0)_{;t}$ and (normalized) amplitude $\hat{a}_i/\hat{a}_0$, plotted *vs.* time, are shown in figure 11. The growth rate rises initially, just as in figure 9, but rather than tending to a plateau, it oscillates with a long period. The mean of these oscillations of the growth rate is zero, as indicated by the plot of the amplitude (the time integral of the growth rate), which does not grow with time.

This simulation and all other elastic simulations we have performed support the principal conclusion of this work: a perturbed frictionless material interface between

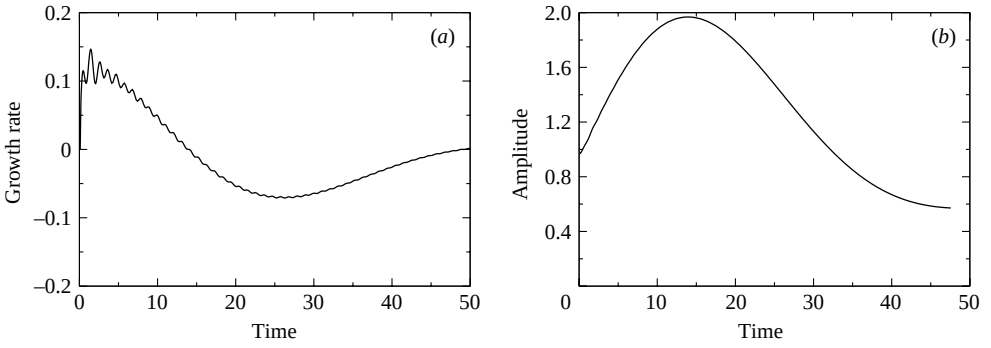

FIGURE 11. Results for a small value of the interpolation parameter ($\kappa = 0.001$). (*a*) Growth rate *vs.* time. (*b*) Amplitude *vs.* time.

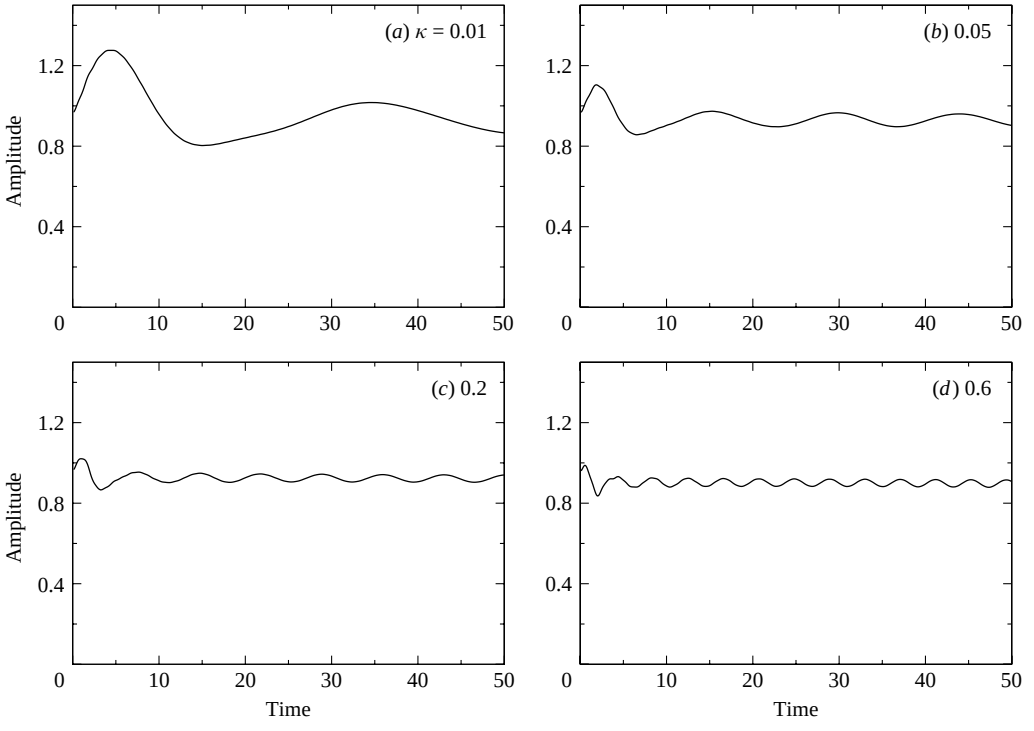

FIGURE 12. Amplitude *vs.* time for intermediate values of the interpolation parameter κ.

elastic materials is not unstable when struck normally by a shock wave. An important consequence is that the linearized theory remains valid at late time.

Next, we increase the material interpolation parameter successively to $\kappa = 0.01$, 0.05, 0.2 and 0.6. The plots of amplitude *vs.* time appear in figure 12. As the values of the shear moduli increase, the (normalized) amplitude $\hat{a}_i/\hat{a}_0$ tends to oscillate with shorter period and smaller peak-to-peak variation around an asymptote. The plot of amplitude *vs.* time for tantalum/aluminium (i.e. $\kappa = 1$) appears in figure 13.

The observed increase of the frequency with the shear moduli is quantified as follows. A scale for frequency is set by the shear moduli; indeed, $k\sqrt{G/\rho}$ has units of frequency. This scale varies as $\sqrt{\kappa}$ in the simulations of figures 12 and 13. For these

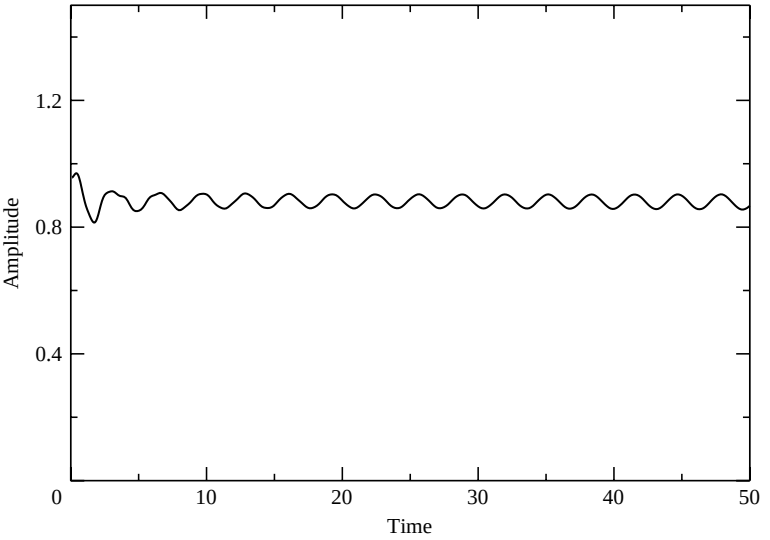

FIGURE 13. Amplitude *vs.* time for tantalum/aluminium for Mach number $\bar{M}_I = 1.076$ of the incident shock wave.

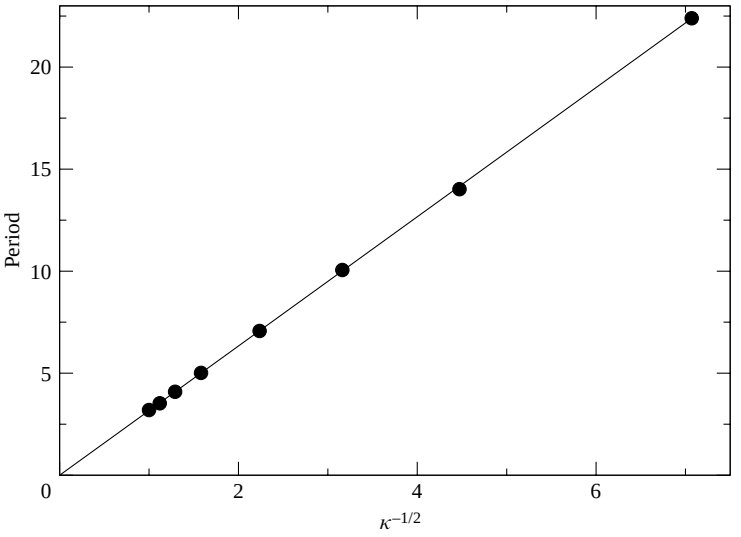

FIGURE 14. Period of oscillations *vs.* $1/\sqrt{\kappa}$ for various values of the interpolation parameter κ.

simulations and others, a plot of the period *vs.* $1/\sqrt{\kappa}$ is fitted very well by a straight line through the origin (see figure 14).

The results are similar for simulations with various incident shock speeds ($\bar{s}_I$ being 6.65, 6.88, 7.00 and 7.27 km s^{-1}, corresponding to Mach numbers $\bar{M}_I = 1.022$, 1.057, 1.076 and 1.116, particle speeds 0.22, 0.54 0.70, and 1.13 km s^{-1}, and pressures 2.8, 7.3, 9.7 and 17.2 GPa), as shown in figure 15. Notice also that the frequency of the oscillations is quite independent of Mach number. Moreover, for a larger shock strength, the amplitude oscillates with a larger peak-to-peak variation about a smaller asymptotic value. This asymptotic value corresponds roughly to the compression

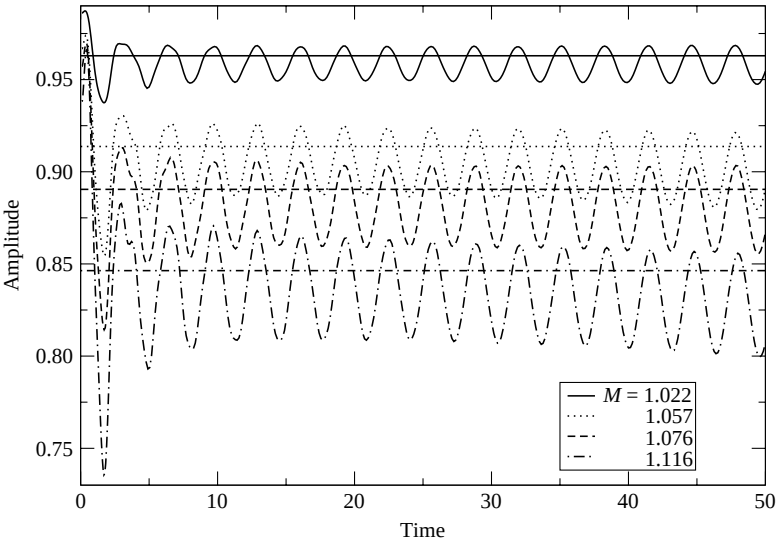

FIGURE 15. Amplitude *vs.* time for tantalum/aluminium and various Mach numbers of the incident shock wave. The lines show the values $(\bar{J}_{3L} + \bar{J}_{3R})\hat{a}_0/2$ corresponding to static compression of the perturbation by the background solutions.

caused by the initial shock wave, as seen from the lines drawn in figure 15 that show the values $(\bar{J}_{3L} + \bar{J}_{3R})\hat{a}_0/2$ that would result from static compression of the perturbation by the background solutions. Larger variation of the amplitude is consistent with a more energetic shock wave.

Remark. These shock strengths are achievable in laboratory experiments. However, the shock pressures far exceed the yield strengths of the materials considered (between 0.01 and 0.17 GPa for aluminium). As our model does not account for plastic behaviour, the simulations are not realistic. Nonetheless, Richtmyer–Meshkov flow for elastic materials is stable even when initiated by shock waves with large strength.

To check the effect of the bulk modulus K_0 on elastic Richtmyer–Meshkov flow, we reduce the values of K_0 to 125 GPa and 50.2 GPa for tantalum and aluminium, respectively. (These values are such that the corresponding longitudinal elastic sound speeds, given by the formula $\sqrt{(K_0 + 4G/3)/\rho}$, equal the bulk sound speeds $\sqrt{K_{0,\mathrm{Ta}}/\rho}$ and $\sqrt{K_{0,\mathrm{Al}}/\rho}$; the shear sound speed are unchanged. The bulk sound speed is roughly the propagation speed of the longitudinal plastic wave in a uniaxial stress flow. Thus, the elastic model has wave speeds that are close to those in the plastic flow regime.) Comparing the result in figure 16 to that in figure 13 shows that changing the bulk modulus has little effect.

We have also observed the following behaviour of the discontinuity in the transverse velocity component, $\hat{v}^2$, at the material interface: for gas dynamics, $\Delta\hat{v}^2$ remains close to its initial value; but for elastic materials, it reduces in size by a substantial factor and subsequently alternates in sign with the same frequency as observed in the amplitude plots (see figure 17.) Notice that the vorticity $\omega_3 = v^2{}_{;1} - v^1{}_{;2}$ has a delta-function singularity at the material interface with coefficient $\Delta\hat{v}^2 \sin(ky)$. Therefore, $\Delta\hat{v}^2$ is essentially the vorticity that drives the roll-up of the material interface.

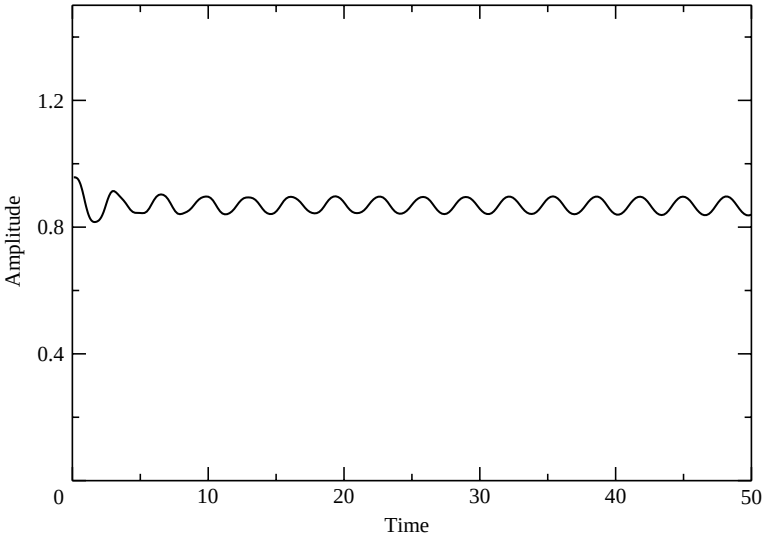

FIGURE 16. Amplitude *vs.* time for tantalum/aluminium with reduced bulk moduli.

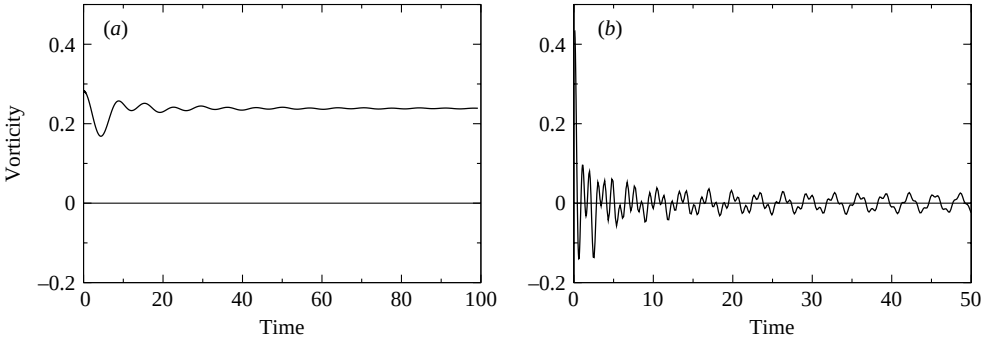

FIGURE 17. Vorticity $\Delta\hat{v}^2$ *vs.* time for gas dynamics and for elasticity. (*a*) Yang–Zhang–Sharp gas problem. (*b*) Tantalum/aluminium with $\bar{s}_I = 6.65$.

This observation suggests an explanation for the stability of Richtmyer–Meshkov flow for elastic materials. The incident shock wave deposits vorticity on the perturbed interface, and this sheet of vorticity is subject to Kelvin–Helmholtz instability. In (inviscid) gas dynamics, the vorticity remains on the interface (it propagates along particle paths), so that Kelvin–Helmholtz instability leads to growth of perturbations. In contrast, for elastic materials, the vorticity propagates at the shear wave speeds ($\boldsymbol{\ell}_2$ and $\boldsymbol{\ell}_6$ are the only eigenvectors with non-zero v^2 components), and is thus carried off the interface. Therefore, perturbations of the interface do not grow.

Finally, we have run simulations of linearized Richtmyer–Meshkov flow for a large variety of pairs of elastic materials. The results are qualitatively similar to those for tantalum/aluminium.

9. Discussion

Although we have not thoroughly explored the large parameter space for the elastic Richtmyer–Meshkov flow problem, our simulations support the following conclusions

concerning the growth rate and amplitude of perturbations of a frictionless material interface between elastic materials when it is struck normally by a shock wave.

(*a*) Even a small shear modulus changes the late-time asymptotic behaviour of the growth rate: rather than approaching a constant, so that the amplitude grows linearly, it oscillates in such a way that the amplitude remains bounded. In particular, the linear theory remains valid at late time.

(*b*) The amplitude oscillates around an asymptotic value with a frequency that grows with the shear moduli and is independent of the strength of the incident shock wave.

(*c*) If the shock strength is increased, the amplitude oscillates about a smaller asymptotic value and the oscillations increase in variation.

(*d*) Varying the bulk modulus has little effect on the behaviour of the material interface.

(*e*) The vorticity on the material interface, which is deposited initially by the incident shock wave, rapidly decays because it is carried off the interface by shear waves.

This work was supported in part by the US Department of Energy. The major part of this work derives from the PhD dissertation of J. N. P., who thanks Professor James Glimm for his inspiration and guidance toward its completion.

Appendix. Explicit formulae

In this Appendix we present the formulae that are specific to the assumptions of either (i) plane-strain perturbed flow or (ii) uniaxial background flow.

A.1. *Plane-strain formulae*

For the general plane-strain form of g_i^α, the non-zero components of $\boldsymbol{F}$ are $F^1{}_1 = Jg^2{}_2$, $F^1{}_2 = -Jg^1{}_2$, $F^2{}_1 = -Jg^2{}_1$, $F^2{}_2 = Jg^1{}_1$ and $F^3{}_3 = 1$, where the Jacobian J is given by

$$J = \left(g^1{}_1 g^2{}_2 - g^1{}_2 g^2{}_1\right)^{-1}. \tag{A 1}$$

Consequently, the non-zero components of $\tilde{\boldsymbol{b}}$ are

$$\tilde{b}^{11} = J^{4/3}\left[\left(g^1{}_2\right)^2 + \left(g^2{}_2\right)^2\right], \tag{A 2}$$

$$\tilde{b}^{12} = \tilde{b}^{21} = -J^{4/3}\left[g^1{}_1 g^1{}_2 + g^2{}_1 g^2{}_2\right], \tag{A 3}$$

$$\tilde{b}^{22} = J^{4/3}\left[\left(g^1{}_1\right)^2 + \left(g^2{}_1\right)^2\right], \tag{A 4}$$

$$\tilde{b}^{33} = J^{-2/3}. \tag{A 5}$$

These formulae allow the computation of

$$\epsilon^2 = \tfrac{1}{2}(\tilde{b}^{11} + \tilde{b}^{22} + \tilde{b}^{33} - 3) \tag{A 6}$$

and the non-zero components of $\operatorname{dev}\tilde{\boldsymbol{b}}$, namely

$$(\operatorname{dev}\tilde{b})^{11} = \tfrac{2}{3}\tilde{b}^{11} - \tfrac{1}{3}\tilde{b}^{22} - \tfrac{1}{3}\tilde{b}^{33}, \tag{A 7}$$

$$(\operatorname{dev}\tilde{b})^{12} = (\operatorname{dev}\tilde{b})^{21} = \tilde{b}^{12}, \tag{A 8}$$

$$(\operatorname{dev}\tilde{b})^{22} = -\tfrac{1}{3}\tilde{b}^{11} + \tfrac{2}{3}\tilde{b}^{22} - \tfrac{1}{3}\tilde{b}^{33}, \tag{A 9}$$

$$(\operatorname{dev}\tilde{b})^{33} = -\tfrac{1}{3}\tilde{b}^{11} - \tfrac{1}{3}\tilde{b}^{22} + \tfrac{2}{3}\tilde{b}^{33}. \tag{A 10}$$

Explicit formulae for ε and σ^{ij} are obtained by substituting the foregoing equations into (2.18) and (2.19), respectively.

A.2. *Flow variables in a uniaxial state*

Next we record the values of flow quantities in a uniaxial state, indicated by a bar. (Evaluation at the uniaxial state simplifies the formulae, and the Richtmyer–Meshkov flow is a perturbation of such a uniaxial state.) The only non-zero components of $\bar{\boldsymbol{g}}$ are $\bar{g}^1{}_1 = \bar{J}^{-1}$, $\bar{g}^2{}_2 = 1$ and $\bar{g}^3{}_3 = 1$, and the only non-zero component of $\bar{v}^i$ is $\bar{v}^1 =: \bar{v}$, so that

$$\bar{\boldsymbol{U}} = [\bar{J}^{-1} \quad 0 \quad 0 \quad 1 \quad \bar{v} \quad 0 \quad \bar{p}]^T. \tag{A 11}$$

We have that $\bar{\rho} = \rho_0 \bar{J}^{-1}$, $\bar{\tau} = \tau_0 \bar{J}$, $\bar{e} = \bar{\varepsilon}_{\text{kinetic}} + \bar{\varepsilon}$, $\bar{\varepsilon}_{\text{kinetic}} = (\bar{v})^2/2$, and $\bar{\varepsilon} = \hat{\varepsilon}_h(\bar{\tau}, \bar{p}) + \bar{\tau} G \bar{\epsilon}^2$, where by (A 2)–(A 6),

$$\bar{\epsilon}^2 = \tfrac{1}{2}\left\{\bar{J}^{4/3} + 2\bar{J}^{-2/3} - 3\right\}. \tag{A 12}$$

In these terms,

$$\bar{\boldsymbol{W}} = \boldsymbol{H}(\bar{\boldsymbol{U}}) = [\bar{J}^{-1} \quad 0 \quad 0 \quad 1 \quad \bar{\rho}\bar{v} \quad 0 \quad \bar{\rho}\bar{e}]^T. \tag{A 13}$$

Moreover, by (A 7)–(A 10), the non-zero components of $\bar{\boldsymbol{\sigma}}$ are

$$\bar{\sigma}^{11} = -\bar{p}_{\text{mean}} + \tfrac{2}{3} G \bar{J}^{-2/3}(\bar{J}^2 - 1), \qquad \bar{\sigma}^{22} = \bar{\sigma}^{33} = -\bar{p}_{\text{mean}} - \tfrac{1}{3} G \bar{J}^{-2/3}(\bar{J}^2 - 1), \tag{A 14}$$

where $\bar{p}_{\text{mean}} = \bar{p} - G\bar{\epsilon}^2$. Therefore, the flux in the x-direction is

$$\boldsymbol{F}(\bar{\boldsymbol{U}}) = [\bar{J}^{-1}\bar{v} \quad 0 \quad 0 \quad 0 \quad \bar{\rho}(\bar{v})^2 - \bar{\sigma}^{11} \quad 0 \quad \bar{\rho}\bar{e}\bar{v} - \bar{v}\bar{\sigma}^{11}]^T \tag{A 15}$$

and the flux in the y-direction is

$$\boldsymbol{G}(\bar{\boldsymbol{U}}) = [0 \quad \bar{J}^{-1}\bar{v} \quad 0 \quad 0 \quad 0 \quad -\bar{\sigma}^{22} \quad 0]^T. \tag{A 16}$$

A.3. *Stress and energy derivatives in a uniaxial state*

Now we calculate the stress derivatives appearing in (2.26), evaluated in a uniaxial state (again indicated by a bar). We also calculate the energy derivatives required in §§A.4 and A.5.

As a preliminary step in calculating the stress derivatives, we note that the non-zero derivatives of $\tilde{b}^{11}$ and $\tilde{b}^{22}$ with respect to $g^\alpha{}_i$, evaluated in a uniaxial state, are

$$\overline{\left.\frac{\partial \tilde{b}^{11}}{\partial g^1{}_1}\right|_p} = -\tfrac{4}{3}\bar{J}^{7/3}, \qquad \overline{\left.\frac{\partial \tilde{b}^{11}}{\partial g^2{}_2}\right|_p} = \tfrac{2}{3}\bar{J}^{4/3}, \tag{A 17}$$

$$\overline{\left.\frac{\partial \tilde{b}^{22}}{\partial g^1{}_1}\right|_p} = \tfrac{2}{3}\bar{J}^{1/3}, \qquad \overline{\left.\frac{\partial \tilde{b}^{22}}{\partial g^2{}_2}\right|_p} = -\tfrac{4}{3}\bar{J}^{-2/3}. \tag{A 18}$$

In particular, we find that the non-zero derivatives of ϵ^2 are

$$\overline{\left.\frac{\partial \epsilon^2}{\partial g^1{}_1}\right|_p} = -\tfrac{2}{3}\bar{J}^{1/3}(\bar{J}^2 - 1), \qquad \overline{\left.\frac{\partial \epsilon^2}{\partial g^2{}_2}\right|_p} = \tfrac{1}{3}\bar{J}^{-2/3}(\bar{J}^2 - 1). \tag{A 19}$$

Noting that $\sigma^{ij} = (-p + G\epsilon^2)\delta^{ij} + G(\operatorname{dev}\tilde{b})^{ij}$ and referring to (A 7)–(A 9), we find that the non-zero derivatives of the stress components, evaluated in a uniaxial state,

are as follows:

$$\overline{\left.\frac{\partial\sigma^{11}}{\partial g^1{}_1}\right|_p} = -\tfrac{2}{9}G\bar{J}^{1/3}(7\bar{J}^2-1), \quad \overline{\left.\frac{\partial\sigma^{11}}{\partial g^2{}_2}\right|_p} = \tfrac{1}{9}G\bar{J}^{-2/3}(7\bar{J}^2-1), \tag{A 20}$$

$$\overline{\left.\frac{\partial\sigma^{12}}{\partial g^1{}_2}\right|_p} = \overline{\left.\frac{\partial\sigma^{21}}{\partial g^1{}_2}\right|_p} = -G\bar{J}^{1/3}, \quad \overline{\left.\frac{\partial\sigma^{12}}{\partial g^2{}_1}\right|_p} = \overline{\left.\frac{\partial\sigma^{21}}{\partial g^2{}_1}\right|_p} = -G\bar{J}^{4/3}, \tag{A 21}$$

$$\overline{\left.\frac{\partial\sigma^{22}}{\partial g^1{}_1}\right|_p} = -\tfrac{2}{9}G\bar{J}^{1/3}(\bar{J}^2-4), \quad \overline{\left.\frac{\partial\sigma^{22}}{\partial g^2{}_2}\right|_p} = \tfrac{1}{9}G\bar{J}^{-2/3}(\bar{J}^2-13), \tag{A 22}$$

$$\overline{\left.\frac{\partial\sigma^{11}}{\partial p}\right|_{g^{\gamma}{}_k}} = -1, \qquad \overline{\left.\frac{\partial\sigma^{22}}{\partial p}\right|_{g^{\gamma}{}_k}} = -1. \tag{A 23}$$

Similarly, from (2.18) and (2.20) we find that the non-zero derivatives of $\rho\varepsilon$ are

$$\overline{\left.\frac{\partial(\rho\varepsilon)}{\partial g^1{}_1}\right|_p} = -\tfrac{2}{3}G\bar{J}^{1/3}(\bar{J}^2-1), \qquad \overline{\left.\frac{\partial(\rho\varepsilon)}{\partial g^2{}_2}\right|_p} = \tfrac{1}{3}G\bar{J}^{-2/3}(\bar{J}^2-1), \qquad \overline{\left.\frac{\partial(\rho\varepsilon)}{\partial p}\right|_{g^{\gamma}{}_k}} = \frac{1}{\Gamma}. \tag{A 24}$$

A.4. *Coefficient matrices in a uniaxial state*

Next we display the coefficient matrices appearing in (4.1), which are read from the quasi-linear equations (2.24), (2.26) and (2.29), as evaluated in a uniaxial state:

$$\boldsymbol{C}(\bar{\boldsymbol{U}}) = \begin{bmatrix} \bar{v} & 0 & 0 & 0 & \bar{J}^{-1} & 0 & 0 \\ 0 & \bar{v} & 0 & 0 & 0 & 0 & 0 \\ 0 & 0 & \bar{v} & 0 & 0 & 1 & 0 \\ 0 & 0 & 0 & \bar{v} & 0 & 0 & 0 \\ -\bar{\tau}\overline{\left.\frac{\partial\sigma^{11}}{\partial g^1{}_1}\right|_p} & 0 & 0 & -\bar{\tau}\overline{\left.\frac{\partial\sigma^{11}}{\partial g^2{}_2}\right|_p} & \bar{v} & 0 & -\bar{\tau}\overline{\left.\frac{\partial\sigma^{11}}{\partial p}\right|_{g^{\gamma}{}_k}} \\ 0 & -\bar{\tau}\overline{\left.\frac{\partial\sigma^{21}}{\partial g^1{}_2}\right|_p} & -\bar{\tau}\overline{\left.\frac{\partial\sigma^{21}}{\partial g^2{}_1}\right|_p} & 0 & 0 & \bar{v} & 0 \\ 0 & 0 & 0 & 0 & \bar{K} & 0 & \bar{v} \end{bmatrix} \tag{A 25}$$

and

$$\boldsymbol{D}(\bar{U}) = \begin{bmatrix} 0 & 0 & 0 & 0 & 0 & 0 & 0 \\ 0 & 0 & 0 & 0 & \bar{J}^{-1} & 0 & 0 \\ 0 & 0 & 0 & 0 & 0 & 0 & 0 \\ 0 & 0 & 0 & 0 & 0 & 1 & 0 \\ 0 & -\bar{\tau}\overline{\left.\frac{\partial\sigma^{12}}{\partial g^1{}_2}\right|_p} & -\bar{\tau}\overline{\left.\frac{\partial\sigma^{12}}{\partial g^2{}_1}\right|_p} & 0 & 0 & 0 & 0 \\ -\bar{\tau}\overline{\left.\frac{\partial\sigma^{22}}{\partial g^1{}_1}\right|_p} & 0 & 0 & -\bar{\tau}\overline{\left.\frac{\partial\sigma^{22}}{\partial g^2{}_2}\right|_p} & 0 & 0 & -\bar{\tau}\overline{\left.\frac{\partial\sigma^{22}}{\partial p}\right|_{g^{\gamma}{}_k}} \\ 0 & 0 & 0 & 0 & 0 & \bar{K} & 0 \end{bmatrix}. \tag{A 26}$$

We have taken note of which matrix entries are zero because a stress derivative vanishes in a uniaxial state, as shown in § A.3.

A.5. *Flux derivatives in a uniaxial state*

Finally, we calculate the quantities appearing as coefficients in the linearized Rankine–Hugoniot conditions, (4.3). The derivative of the conserved quantity is

$$\boldsymbol{H}'(\bar{\boldsymbol{U}}) = \begin{bmatrix} 1 & 0 & 0 & 0 & 0 & 0 & 0 \\ 0 & 1 & 0 & 0 & 0 & 0 & 0 \\ 0 & 0 & 1 & 0 & 0 & 0 & 0 \\ 0 & 0 & 0 & 1 & 0 & 0 & 0 \\ \rho_0\bar{v} & 0 & 0 & \bar{\rho}\bar{v} & \bar{\rho} & 0 & 0 \\ 0 & 0 & 0 & 0 & 0 & \bar{\rho} & 0 \\ H'(\bar{\boldsymbol{U}})_{71} & 0 & 0 & H'(\bar{\boldsymbol{U}})_{74} & \bar{\rho}\bar{v} & 0 & H'(\bar{\boldsymbol{U}})_{77} \end{bmatrix}, \tag{A 27}$$

where

$$H'(\bar{\boldsymbol{U}})_{71} = \rho_0\bar{\varepsilon}_{\text{kinetic}} + \overline{\left.\frac{\partial(\rho\varepsilon)}{\partial g^1{}_1}\right|_p}, \quad H'(\bar{\boldsymbol{U}})_{74} = \bar{\rho}\bar{\varepsilon}_{\text{kinetic}} + \overline{\left.\frac{\partial(\rho\varepsilon)}{\partial g^2{}_2}\right|_p}, \tag{A 28}$$

$$H'(\bar{\boldsymbol{U}})_{77} = \overline{\left.\frac{\partial(\rho\varepsilon)}{\partial p}\right|_{g^{\gamma}{}_k}}. \tag{A 29}$$

The derivative of the flux in the x-direction is

$$\boldsymbol{F}'(\bar{\boldsymbol{U}}) = \begin{bmatrix} \bar{v} & 0 & 0 & 0 & \bar{J}^{-1} & 0 & 0 \\ 0 & 0 & 0 & 0 & 0 & 0 & 0 \\ 0 & 0 & \bar{v} & 0 & 0 & 1 & 0 \\ 0 & 0 & 0 & 0 & 0 & 0 & 0 \\ F'(\bar{\boldsymbol{U}})_{51} & 0 & 0 & F'(\bar{\boldsymbol{U}})_{54} & 2\bar{\rho}\bar{v} & 0 & F'(\bar{\boldsymbol{U}})_{57} \\ 0 & F'(\bar{\boldsymbol{U}})_{62} & F'(\bar{\boldsymbol{U}})_{63} & 0 & 0 & \bar{\rho}\bar{v} & 0 \\ F'(\bar{\boldsymbol{U}})_{71} & 0 & 0 & F'(\bar{\boldsymbol{U}})_{74} & F'(\bar{\boldsymbol{U}})_{75} & 0 & F'(\bar{\boldsymbol{U}})_{77} \end{bmatrix}, \tag{A 30}$$

where

$$F'(\bar{\boldsymbol{U}})_{51} = \rho_0(\bar{v})^2 - \overline{\left.\frac{\partial\sigma^{11}}{\partial g^1{}_1}\right|_p}, \quad F'(\bar{\boldsymbol{U}})_{54} = \bar{\rho}(\bar{v})^2 - \overline{\left.\frac{\partial\sigma^{11}}{\partial g^2{}_2}\right|_p}, \quad F'(\bar{\boldsymbol{U}})_{57} = -\overline{\left.\frac{\partial\sigma^{11}}{\partial p}\right|_{g^{\gamma}{}_k}}, \tag{A 31}$$

$$F'(\bar{\boldsymbol{U}})_{62} = -\overline{\left.\frac{\partial\sigma^{21}}{\partial g^1{}_2}\right|_p}, \quad F'(\bar{\boldsymbol{U}})_{63} = -\overline{\left.\frac{\partial\sigma^{21}}{\partial g^2{}_1}\right|_p}, \tag{A 32}$$

$$F'(\bar{\boldsymbol{U}})_{71} = \rho_0\bar{\varepsilon}_{\text{kinetic}}\bar{v} + \overline{\left.\frac{\partial(\rho\varepsilon)}{\partial g^1{}_1}\right|_p}\bar{v} - \bar{v}\,\overline{\left.\frac{\partial\sigma^{11}}{\partial g^1{}_1}\right|_p}, \tag{A 33}$$

$$F'(\bar{\boldsymbol{U}})_{74} = \bar{\rho}\bar{\varepsilon}_{\text{kinetic}}\bar{v} + \overline{\left.\frac{\partial(\rho\varepsilon)}{\partial g^2{}_2}\right|_p}\bar{v} - \bar{v}\,\overline{\left.\frac{\partial\sigma^{11}}{\partial g^2{}_2}\right|_p}, \tag{A 34}$$

$$F'(\bar{\boldsymbol{U}})_{75} = \bar{\rho}(\bar{v})^2 + \bar{\rho}\bar{e} - \bar{\sigma}^{11}, \quad F'(\bar{\boldsymbol{U}})_{77} = \overline{\left.\frac{\partial(\rho\varepsilon)}{\partial p}\right|_{g^{\gamma}{}_k}}\bar{v} - \bar{v}\,\overline{\left.\frac{\partial\sigma^{11}}{\partial p}\right|_{g^{\gamma}{}_k}}. \tag{A 35}$$

REFERENCES

Adams, G. G. 1995 Self-excited oscillations of two elastic half-spaces sliding with a constant coefficient of friction. *J. Appl. Mech.* **62**, 867–872.

Courant, R. & Friedrichs, K. 1976 *Supersonic Flow and Shock Waves*. Springer.

Dafermos, C. 2000 *Hyperbolic Conservation Laws in Continuum Physics*. Springer.

Grove, J., Holmes, R., Sharp, D., Yang, Y. & Zhang, Q. 1993 Quantitative theory of Richtmyer–Meshkov instability. *Phys. Rev. Lett.* **71**, 3473–3476.

Gurtin, M. 1981 *An Introduction to Continuum Mechanics*. Academic.

Holmes, R. L. 1994 A numerical investigation of the Richtmyer–Meshkov instability using front tracking. PhD thesis, State University of New York at Stony Brook.

LeVeque, R. 1992 *Numerical Methods for Conservation Laws*. Birkhäuser.

Marsden, J. & Hughes, T. 1983 *Mathematical Foundations of Elasticity*. Prentice–Hall.

Menikoff, R. & Plohr, B. 1989 The Riemann problem for fluid flow of real materials. *Rev. Mod. Phys.* **61**, 75–130.

Meshkov, E. 1970 Instability of a shock wave accelerated interface between two gases. *NASA Tech. Trans.* **F-13**, 074.

Nam, J. 2001 Linearized analysis of the Richtmyer–Meshkov instability for elastic materials. PhD thesis, State University of New York at Stony Brook.

Plohr, B. & Sharp, D. 1988 A conservative Eulerian formulation of the equations for elastic flow. *Adv. Appl. Maths* **9**, 481–499.

Plohr, B. & Sharp, D. 1992 A conservative formulation for plasticity. *Adv. Appl. Maths* **13**, 462–493.

Plohr, B. & Sharp, D. 1998 Instability of accelerated elastic metal plates. *Z. angew. Math. Phys.* **49**, 786–804.

Richtmyer, R. 1960 Taylor instability in shock acceleration of compressible fluids. *Commun. Pure Appl. Maths* **13**, 297–319.

Rupert, V. 1992 Shock–interface interaction: current research on the Richtmyer–Meshkov problem. In *Shock Waves, Proc. of the 18th Intl Symp. on Shocks Waves* (ed. K. Takayama). Springer.

Simo, J. & Hughes, T. 1998 *Computational Inelasticity*. Springer.

Smoller, J. 1994 *Shock Waves and Reaction–Diffusion Equations*, 2nd edn. Springer.

Strikwerda, J. 1989 *Finite Difference Schemes and Partial Differential Equations*. Wadsworth & Brooks/Cole, Pacific Grove, CA.

Trangenstein, J. & Colella, P. 1991 A higher-order Godunov method for modeling finite deformation in elastic–plastic solids. *Commun. Pure Appl. Maths* **44**, 41–100.

Wagner, D. 1996 Conservation laws, coordinate transformations, and differential forms. In *Proc. of the Fifth Intl Conf. on Hyperbolic Problems Theory, Numerics, and Applications* (ed. J. Glimm, M. J. Graham, J. W. Grove & B. J. Plohr), pp. 471–477. World Scientific Publishers, Singapore.

Walter, J., Glimm, J., Grove, J., Hwang, H.-C., Lin, X., Plohr, B., Sharp, D. & Yu, D. 1999 Eulerian front tracking for solid dynamics. In *Proc. of the 15th US Army Symp. on Solid Mechanics* (ed. K. Iyer & S. Chin Chou), pp. 343–366. Battelle Memorial Institute, Myrtle Beach, SC. Battelle Press (www.battelle.org/bookstore), published on CD-ROM (ISBN 1-57477-083-7).

Yang, Y., Zhang, Q. & Sharp, D. 1994 Small amplitude theory of Richtmyer–Meshkov instability. *Phys. Fluids* **6**, 1856–1873.

Zhang, Q. & Graham, M. J. 1998 A numerical study of Richtmyer–Meshkov instability driven by cylindrical shocks. *Phys. Fluids* **10**, 974–992.